Effects of High Strength Concrete on Progressive Collapse Resistance of Reinforced Concrete Frame

Xiao-Fang Deng[1], Shi-Lin Liang[2], Feng Fu[3], C.Eng, M.ASCE and Kai Qian[4] Ph.D, M.ASCE

ABSTRACT

The application of extreme loads such as impact and blast may lead to progressive collapse and the robustness of a structure must be considered in this context. Although extensive studies had been carried out over the past decades to study the load resisting mechanism of reinforced concrete (RC) frames to prevent progressive collapse, the effects of high-strength-concrete (HSC) on progressive collapse resistance capacity is still unclear. Therefore, six tests of RC frames with different span-to-depth ratio and concrete strength were conducted in present study. Among them, three are HSC frames and the remaining are normal strength concrete frames. It was found that the use of HSC could further enhance the compressive arch action (CAA) capacity, especially for those with low span-to-depth ratio. On the other hand, HSC can reduce the tensile catenary action (TCA) capacity at large deformation stage, primarily because of higher bond stress between concrete and rebar, leading to earlier fracture of the rebar. The analytical results from the model were compared with the test results. It was found that the refined CAA model could accurately predict the CAA capacity of NSC frames, but not for HSC frames. Moreover, existing model is hard to predict the CAA capacity of the frames with relatively small span-to-depth ratio (less than 7) accurately.

CE Database subject heading: progressive collapse; high strength concrete; compressive arch action; tensile catenary action

---

[1] Assistant Professor in College of Civil Engineering and Architecture at Guangxi University, China, 530004, xiaofang.deng@gxu.edu.cn

[2] Research Student in College of Civil Engineering and Architecture at Guangxi University, China, 530004, liangshilin@st.gxu.edu.cn

[3] Senior Lecturer in Structural Engineering, School of Mathematics, Computer Science and Engineering, City, University of London, U.K., Feng.Fu.1@city.ac.uk
[4]Professor in College of Civil Engineering and Architecture at Guangxi University, China, 530004, (corresponding author) qiankai@gxu.edu.cn

INTRODUCTION

Buildings may subject to initial local damage due to intended or accidental events, such as the loss of one or a couple of columns. However, in ordinary civilian building design, the column missing is not well considered in the past design guidelines. Therefore, these buildings may have high risk to propagate initial local damage disproportionately to a large area of the building or even cause entire collapse. The terminology of progressive collapse is first proposed after the collapse of Ronan Point in 1968. The collapse of Murrah Federal Building in 1995 and Twin-Tower of World Trade Center in 2001 re-sparkled the interest on progressive collapse in academic and practical engineer's communities. Several design codes or guidelines (BS8110 1997; BSI 2006; GSA 2009; ASCE/SEI 7 2010; DoD 2009; ACI-318 2014) were issued for progressive collapse design using so-called explicitly or implicitly design methods. Among them, Alternate Load Path method is commonly accepted for evaluation of the capacity of a building to mitigate progressive collapse due to its threat independent feature.

Based on Alternate Load Path method, extensive tests had been carried out in the past decades to understand the capacity of reinforced concrete (RC) frames to resist progressive collapse. These tests could be categorized into three groups: multi-story tests (Yi et al. 2008; Sasani et al. 2011a; Xiao et al. 2015; Qian and Li 2017; Qian et al. 2019), single-story beam-column or beam-column-slab subassembly tests (Su et al. 2009; Orton et al. 2009; Qian and Li 2012a; FarhangVesali et al. 2013; Yu and Tan 2013a; Lew et al. 2014; Valipour et al. 2015a; Qian et al. 2016; Ren et al. 2016; Peng et al. 2017; Qian et al. 2018), and single-story beam-column connections tests (Qian and Li 2012b; Yu et al. 2014). Yi et al. (2008) carried out a 1/3-scaled three-story planar frame test to evaluate the load resisting mechanism of RC frame subjected to the loss of an interior column. Compressive arch action (CAA) and tensile catenary action (TCA) were found to be the primary mechanisms in resisting progressive collapse at different stages. Sasani et al. (2011a) conducted a real time removal test to study the dynamic response of an 11-story building, which was planned to be demolished, subjected to sudden removal of four adjacent ground columns due to explosives. Flexural beam action and Vierendeel action were identified as the two primary load resisting mechanisms. Xiao et al. (2015) experimentally investigated the dynamic response of a half-scaled three-story RC building, which is deliberately built for progressive collapse study, subjected to different column missing scenarios. The load resisting mechanism shifted from flexural moment resisting to TCA mechanism was observed when two ground exterior columns were removed simultaneously. Qian and Li (2017) tested a series of six three-story frames with or without infilled walls to quantify the effects of masonry infilled walls on load resisting mechanism and capacity of RC frames to resist progressive collapse. It was found that masonry infilled walls enhance the initial stiffness and increase the first peak load significantly. Moreover, the crushing of masonry infilled walls will not jeopardize the development of TCA of the beam at large deformation stage. Qian et al. (2019) also tested another series of five three-story frames to quantify the efficiency of using steel bracings in strengthening RC frames to mitigate progressive collapse. Different configurations of steel bracings were applied. It was found that compressive bracings prone to out-of-plane buckling and have little contribution to the collapse resistance, while tensile bracings may fracture before the development of TCA.

Actually, majority of existing tests on progressive collapse investigation were focused on beam-column substructures or beam-column-slab substructures. This is because it is easier to replicate the boundary conditions and measure the response. Dynamic effects and dynamic load increase factor of RC frames subjected to sudden column removal scenario were also investigated (Qian and Li 2012b; Yu et al. 2014; Peng et al. 2017). These literatures documented that the failure mode and resistance of the specimens were similar to their counterparts tested in a static test manner. Moreover, the behavior of beam-column connections subjected to different column missing scenarios were evaluated experimentally by Yap and Li (2011) and Qian and Li (2012c), which could provide sufficient evidence for the level of confidence in simplification of the boundary conditions in substructure tests.

The load resisting mechanisms of bare RC frames subjected to middle column missing scenario were quantified by pushdown test methods (Su et al. 2009; FarhangVesali et al. 2013; Valipour et al. 2015a). Su et al. (2009) concluded that loading rate has little effect on CAA capacity. FarhangVesali et al. (2013) reported that longitudinal reinforcement ratio and stirrup configuration have a minor effect on the CAA. Valipour et al. (2015a) experimentally investigated the effects of concrete strength (ranging from 18 MPa to 67 MPa) on the CAA of RC beam assemblages. The test results demonstrated that the concrete strength has significant influence on the peak load capacity (CAA capacity) of the tested specimens. The stiffness of supports also has significant effects on mobilization of CAA. Valipour et al. (2015b) filled knowledge gap in progressive collapse response of RC frame using steel fiber to replace conventional transverse reinforcements, the test results demonstrated that the replacement had little effects on the development of TCA. The role of slabs, compressive membrane action (CMA) and tensile membrane action (TMA) developed in RC slabs were evaluated (Qian and Li 2012a; Qian et al. 2016; Ren et al. 2016). It was found that, the CMA and TMA bring great benefit to the resistance. The CMA capacity was affected by the stiffness of boundary elements and strength of concrete significantly while the TMA capacity was mainly affected by the amount of slab reinforcement in bottom layer (continual). Moreover, improving CMA of precast concrete slabs to resist wheel loading using additional transverse confining system (i.e., straps, cross-bracing and a combination of straps and cross-bracing) was reported by Valipour et al. (2015c). It was found that the peak load capacity could be enhanced significantly due to considerable restraint provided by the confining system. Furthermore, the effects of seismic design and detailing on behavior of RC moment frames to resist progressive collapse were evaluated (Choi and Kim 2011, Qian and Li 2012c, Kim and Choi 2016, Lu et al. 2017). Choi and Kim (2011) and Kim and Choi (2016) indicated that seismically designed specimens performed much better than the corresponding non-seismically designed specimens as seismically designed specimens had higher reinforcement ratio and transverse reinforcement installed at joint zones, which delayed the failure of exterior joints. Lu et al. (2017) found that for normal strength concrete frames, seismically design could increase the beam longitudinal reinforcement ratio, which resulted in a much larger resistance in both beam and catenary action. However, the increase of beam depth could improve the resistance of beam action but not the catenary action. Moreover, the results from Kim et al. (2011) indicated that rotational friction damper, which was normally for mitigating seismic or wind load, was also effectively improve the behavior of RC frames to mitigate progressive collapse.

Although above studies had deeply improved the understanding on load resisting mechanisms of RC frames to resist progressive collapse, these studies are mainly focused on normal strength concrete (NSC). As high strength concrete (HSC) has advantages in load resisting capacity enhancement, smaller member size, less self-weight etc, HSC is widely used in high-rise buildings in the past decades. Moreover, the high-rise buildings have higher possibility for terrorism attacks due to their higher social impact caused by attacks. Thus, it is necessary to evaluate the behavior of reinforced HSC frames to resist progressive collapse and to identify the effects of HSC on load resisting mechanism of RC frames. For this purpose, a series of six RC frames, using both HSC and NSC, were designed and tested under pushdown loading regime. The accuracy of existing analytical models in predicting CAA and TCA of HSC frames was also evaluated.

DESCRIPTION OF TEST PROGRAM

Experimental specimens

Six half-scaled beam-column sub-assemblages were designed and constructed to evaluate the effects of HSC on behavior of RC frames to resist progressive collapse. These specimens include three HSC specimens (HSC-13, HSC-11, and HSC-8) and three NSC specimens (NSC-13, NSC-11, and NSC-8). The specimens are denoted flows below conventions:

1. 'HSC' represents specimens using HSC and 'NSC' represents specimens using NSC;
2. Number after hyphen denotes span/depth ratio, which is defined by the ratio of clear beam span to its depth.

Fig. 1 shows the dimension and reinforcement details of specimen NSC-11 while Table 1 lists the key properties of the specimens. As shown in Fig. 1, Specimen NSC-11 was non-seismically designed in accordance with ACI 318-14 (2014) with clear span of 2750 mm and beam cross-section of 250 mm×150 mm. The bottom rebar is continuous 2T12 reinforcement, while curtailment is considered for top rebar. The beam transverse reinforcement is R6@100 mm throughout the whole beam without transverse reinforcements in the joint zone. The clear cover of the concrete for beam and column are both 15 mm. T12 and R6 herein represent deformed reinforcement with diameter of 12 mm and plain reinforcement with diameter of 6 mm, respectively. Two beams, one middle column stub, and two enlarged side column stubs were casted. The enlarged side column has dimension of 400 mm×400 mm to replicate fixed boundary conditions following previous studies (Orton et al. 2009; Su et al. 2009; Yu and Tan 2013a).

As tabulated in Table 1, Specimens NSC-13 and NSC-8 have similar reinforcement ratio and beam cross-section to Specimen NSC-11 but clear span of 3250 mm and 2000 mm, respectively. Specimens HSC-13, HSC-11, and HSC-8 have identical dimensions and reinforcement details to NSC counterparts but high strength concrete is used. According to cylindrical compression tests, at the day of test, the recorded concrete compressive strength of NSC-13, NSC-11, NSC-8, HSC-13, HSC-11, and HSC-8 are 30.5 MPa, 31.1 MPa, and 31.7 MPa, 59.3 MPa, 61.2 MPa, and 60.5 MPa, respectively. Based on tensile splitting tests, the tensile strength of the concrete of NSC-13, NSC-11, NSC-8, HSC-13, HSC-11, and HSC-8 are 2.9 MPa, 3.0 MPa, 2.9 MPa, 6.0 MPa, 6.1 MPa, and 6.1 MPa, respectively. Moreover, the properties of reinforcement are tabulated in Table 2.

Test Setup and instrumentations

Similar to previous studies (Orton et al. 2009; Su et al. 2009; Yu and Tan 2013a), as shown in Fig. 2a, fixed boundary condition was replicated at the side column by using two rollers and one bottom pin. To eliminate the redundant horizontal restraints from the bottom pin, a series of steel rollers were placed below the pin support. Therefore, the side columns were statically determinate and the horizontal and vertical reaction force could be measured directly. It is intentionally designed with no middle column at ground level due to desired element removal before applying vertical load. The column removal effect is implemented through a hydraulic jack with a downward stroke of 700 mm. Displacement-controlled method was adopted with a rate of 0.5 mm/s throughout the tests. To prevent out-of-plane failure, a specially designed steel assembly was installed below the hydraulic jack. As illustrated in Fig. 2b, two load cells were installed above and below the hydraulic jack to measure the vertical load (average value was used for final test results records hereafter). In addition, load cell was installed below each pin support to monitor the load redistribution of the columns. Tension/compression load cell (Item 5 in Fig. 2b) was installed in each horizontal roller to measure the horizontal reaction force. A series of linear variable displacement transducers (LVDTs) were installed along the beam (D1 to D7) to monitor the deformation shape during test. LVDTs (H1 and H2) were also installed horizontally at the side columns to determine the stiffness of the horizontal restraints as gap allowance was inevitable when installation of the appliance. Strain gauges were mounted along the length of beam longitudinal reinforcements before casting.

EXPERIMENTAL RESULTS

General behavior

NSC-series: Fig. 3a shows the vertical load-displacement curve of NSC-series specimens and Fig. 4a shows the development of crack pattern of NSC-11. For NSC-11, first crack occurred at the beam ends when the middle joint displacement (MJD) reached 9 mm. When the MJD reached 36 mm, the yield load of 37 kN was obtained. However, the calculated yield strength due to pure bending resistance was 35 kN, which was less than the measured one. This was mainly because of the inherent compressive axial force in reality is not taken into consideration in the analytical model. Further increasing the MJD, the CAA capacity of 52 kN was observed at an MJD of 90 mm, which is called peak displacement in this study. As shown in Fig. 4a, at this loading stage, concrete crushing was observed at the beam ends. The ratio of CAA capacity to yield load is about 1.41, which is due to strain hardening of reinforcements and the mobilization of CAA. After that, the load resistance began to drop gradually due to concrete crushing and second-order effects. However, the load resistance began to re-ascend when the MJD reached 288 mm (about $0.1l_n$) due to the start of TCA. As shown in Fig. 4a, penetrated cracks occurred at this stage. Further increasing displacement, more penetrated cracks were observed which were uniformly distributed along the beam length. The drop of load resistance was due to fracture of bottom rebar in the region of the beam-middle column interface. The TCA capacity of 94 kN was obtained at an MJD of 712 mm. After that, the load resistance suddenly dropped significantly because the complete fracture of the top rebar near the beam-middle column joint. Fig. 5 shows the failure mode of NSC-11. As shown in the figure, severe concrete crushing occurred at the beam ends while rebar fracture occurred primarily at beam end near middle joint region. Penetrated cracks were uniformly distributed along the beam.

For NSC-13 and NSC-8, similar crack pattern and global behavior were observed. The yield load of NSC-13 and NSC-8 was 33 kN and 53 kN, respectively. The calculated yield load of NSC-13 and NSC-8 was 30 kN and 48 kN, respectively based on the analytical model. Similarly, the calculated yield load is less than the measured one, which is primarily due to ignorance of compressive axial force. For NSC-13, the CAA capacity of 43 kN was measured at an MJD of 108 mm. However, for NSC-8, the CAA capacity was 77 kN, which was about 179 % and 148 % of that of NSC-13 and NSC-11, respectively. Moreover, the TCA capacity of NSC-13 and NSC-8 was 81 kN and 88 kN, respectively whereas the deformation capacity of NSC-13 and NSC-8 was 731 mm and 581 mm, respectively. Although the TCA capacity of NSC-13 was less than that of NSC-11 and similar deformation capacity was measured for them as shown in Fig. 3a. The test of NSC-13 was forced to stop due to limited stroke capacity of the jack, rather than the failure of the specimen. If the jack had larger stroke capacity, the deformation capacity and TCA capacity of NSC-13 would have been larger. Figs. 6 and 7 show the failure modes of NSC-13 and NSC-8. In general, the failure mode of NSC-13 was similar to that of NSC-11. However, different to NSC-11 and NSC-13, the diagonal shear cracks along the beams of NSC-8 were observed, rather than flexural cracks perpendicular to the beam axis. This indicated the shear failure in this test.

HSC-series: Fig. 3b shows the vertical load-middle joint displacement curve of HSC-series specimens. For HSC-11, first cracks occurred at the beam ends when the MJD reached 15 mm. At an MJD of 28 mm, yield load of 42 kN, which was 114 % of that of NSC-11, was obtained. Further increasing MJD to 74 mm, the CAA capacity of 60 kN, which was 115 % of that of NSC-11, was achieved. The TCA capacity and deformation capacity of HSC-11 were 80 kN and 663 mm respectively, less than these of NSC-11. The smaller deformation capacity in HSC-11 is mainly due to high strength concrete resulted in high bond strength between reinforcement and concrete, which led to stress concentration and rebar fracture in the tests. Fig. 4b shows the crack pattern of HSC-11. Compared to NSC-11, it can be found that the high strength concrete has little effects on crack development. The failure mode of HSC-11 is shown in Fig. 8, which is similar to that of NSC-11. As shown in Fig. 3b and Table 3, due to larger span/depth ratio, HSC-13 only achieved yield load and CAA capacity about 86 % and 80 % of these of HSC-11. Similar to normal strength concrete, HSC-13 experienced larger deformation. The lower TCA capacity of HSC-13 was caused by the insufficient stroke capacity during the tests. On the contrast, for HSC-8, its yield load capacity and CAA capacity were 133 % and 152 % of these of HSC-11. Different to rest specimens, the TCA capacity of HSC-8 is less than its CAA capacity, which will be further discussed in analytical section of this paper. The failure mode of HSC-13 and HSC-8 are illustrated in Figs. 9 and 10, respectively. For HSC-13, only bottom rebar near the middle joint were fractured. For HSC-8, both bottom and top rebar near the middle joint were fractured.

Horizontal reaction

The horizontal reaction force v.s. middle joint displacement curves are shown in Fig. 11. As shown in Fig. 11a, the horizontal compressive force increased with the increase of vertical displacement. For NSC-11, the horizontal compressive force was -70 kN at yield displacement, which explains the reason that the calculated yield load is less than the measured one. The maximum horizontal compressive force was -178 kN at an MJD of 180 mm, which was greater than the corresponding peak displacement. Then, the horizontal compressive force began to decline with further increase of the displacement. The horizontal compressive force transferred to horizontal tensile force after the MJD of 356 mm. The maximum horizontal tensile force of 154 kN was measured at the MJD of 699 mm. Similar behavior was observed for NSC-13 and NSC-8. The maximum horizontal compressive force of NSC-13 and NSC-8 were -153 kN and -202 kN, respectively. Thus, when span/depth ratio reduced from 11 to 8, the maximum horizontal compressive force increased by 13.4 %. Conversely, increasing the span/depth ratio from 11 to 13, the maximum horizontal compressive force decreased by over 14.0 %. Moreover, the maximum horizontal tensile force of NSC-13 and NSC-8 were 148 kN and 147 kN, respectively. Thus, span/depth ratio will not affect the development of horizontal tensile force.

As shown in Fig. 11b, the maximum horizontal compressive force of HSC-11, HSC-13, and HSC-8 were -259 kN, -233 kN, and -321 kN, respectively. Thus, when span/depth ratio decreased from 11 to 8, the maximum horizontal compressive force was increased by 23.9 %, which was greater than that of the NSC specimens. For the maximum horizontal tensile force, similar to NSC specimens, the span/depth ratio will not affect it significantly.

Deflection shape of beams

Fig. 12 shows the beam deflection shape of NSC-11 in accordance with different critical stages: yield load capacity, CAA capacity, onset of TCA, fracture of rebar, and ultimate deformation. As shown in the figure, from the beginning of the test, the beams exhibit double-curvature deflection shape. Before fracture of the first rebar near the middle joint, the beams' deformation was almost symmetric. Then, the middle joint continued to rotate and the damage prone to be concentrated in the left side of the middle joint due to the weld failure between the top of the middle stub and the steel column, which released the rotational restraints at the middle joint. Moreover, at the final stage of test, the chord rotation, which is defined as ratio of MJD to beam span, was compared with the beam deformation shape. It can be seen that the chord rotation will over-estimate the actual end rotation of the beam end near the side columns while it could estimate the rotation of the beam end near the middle joint well. For other specimens, similar results were observed.

Strain gauge results

Figs. 13a and b show the variation of strain gauge readings along beam top and bottom longitudinal reinforcements of NSC-11, respectively. As shown in the figure, the bottom reinforcement near the middle joint was first yielded. At CAA stage, plastic hinges were formed at both beam ends. However, the compressive strain in both top and bottom rebar began to decline after onset of the TCA stage. At ultimate load stage, no compressive strain was measured at both top and bottom beam longitudinal reinforcement. As shown in Fig. 14, the strain variation of HSC-11 was quite similar to that of NSC-11. However, as shown in Fig. 15, at ultimate load stage, considerable compressive strain was still measured at bottom reinforcement of HSC-8. This could be explained as the high bond between concrete and rebar as well as low span-depth ratio resulted in earlier fracture of longitudinal rebar and delayed the development of tensile strain in rebar.

ANALYSIS AND DISCUSSIONS

Dynamic response of tested specimens

As progressive collapse is a dynamic event due to the sudden column removal, it was worthwhile to evaluate the dynamic capacity of test specimens. Based on the investigation from Qian and Li (2015a, b) and Tsai (2010), an energy-based simplified single-degree-of-freedom (SDOF) model, first proposed by Izzuddin et al. (2008), is accurate for dynamic assessment. Thus, in this study, the energy-based model was utilized to assess the dynamic capacity of specimens based on the measured quasi-static load-displacement curves from the tests. The mathematic equations were expressed as:

$$P_d(u_d) = \frac{1}{u_d}\int_0^{u_d} P_{NS}(u)du \qquad (1)$$

where $P_d(u)$ and $P_{NS}(u)$ are the dynamic capacity and the nonlinear static loading estimated at the displacement demand *u*, respectively.

Fig. 16 shows the dynamic response curves of tested specimens. As shown in the figure, the dynamic ultimate capacity of NSC-13, HSC-13, NSC-11, HSC-11, NSC-8, and HSC-8 were 44 kN, 43 kN, 53 kN, 53 kN, 64 kN, and 78 kN, respectively. Thus, the higher strength concrete has little effects on dynamic ultimate capacity of the specimens with moderate or large span/depth ratio. This is primarily because TCA governs the failure. However, for specimens with small span/depth ratio, high strength concrete could increase the dynamic ultimate capacity significantly as CAA governs the load.

De-composition of the load resistance contribution from axial force and bending moment

To de-composite the resistance contribution from the axial force and bending moments, a series of analyses were carried out. As shown in Fig. 17, only left bay was extracted for analysis due to symmetry. The load resistance *P* could be determined as the summation of the vertical components of the shear force (*V*) and axial force (*N*) at the middle joint when the MJD was δ.

$$P = (Nsin\theta + V\cos\theta) \tag{2}$$

where θ is the rotation of the beam end near the middle joint and can be determined by the vertical displacements ($\theta = \arctan\left(\frac{4(D_4 - D_3)}{l}\right)$); D_3 is the vertical displacement measured at the position with l/4 from the middle joint, and D_4 is the MJD; l is beam span length.

As shown in Fig. 17, *N* and *V* could be determined by the measured horizontal and vertical reaction force at the supports:

$$N = (F_L \tan\theta + H_t + H_b)\cos\theta \tag{3}$$

$$V = (F_L - N\sin\theta)/\cos\theta \tag{4}$$

Therefore, the bending moment at the beam end near the middle column (M_M) and the one near the side column (M_S) could be expressed as:

$$M_M = F_L l - H_t(\delta + 0.35) - H_b(\delta - 0.35) \tag{5}$$

$$M_S = 0.2F_L - 0.35H_t + 0.35H_b \tag{6}$$

where H_t and H_b are the horizontal reaction force at the upper roller and bottom roller, respectively; F_L is the vertical reaction force at the left side column.

NSC-11, HSC-11, NSC-8 and HSC-8 were selected to show the de-composition of load resistance, as shown in Fig. 18. As shown in the figure, initially the contribution from axial force is negative due to development of compressive force at CAA stage. At this stage, the load resistance mainly attributed to the shear force. When tensile force mobilized at TCA stage, the contribution of axial force increased with increase of MJD. However, as shown in the figure, the contribution from shear force is still significant although the contribution from shear force is decreasing with the increase of MJD. Thus, it is not correct to assume the load resistance purely provided from tension force of reinforcement at TCA stage.

Figs. 19a, b, c and d show the variation of bending moment of NSC-11, HSC-11, NSC-8 and HSC-8, respectively. As shown in the figure, the bending moments were much larger than expected pure flexural induced bending moments due to compressive force developed in the beams. Moreover, the maximum bending moment and maximum compressive axial force achieved at the same MJD. For NSC-11, the maximum bending moments near the middle column and near the side column were 46.7 kN·m and 48.7 kN·m, respectively. Compared with NSC-11, the maximum bending moments of HSC-11 were increased by 36.2 % and 38.8 %, respectively. Similarly, compared to NSC-8, the bending moment near the middle column and side column of HSC-8 were increased by 34.3 % and 12.2 %, respectively.

The measured M-N curves of NSC-11, NSC-8, HSC-11, and HSC-8 were presented in Figs. 20, 21, 22, and 23, respectively. It was found that the M-N curves were similar to the theoretical M-N curves for both NSC and HSC specimens. When the bending moment reached its maximum value, the bending moment began to decrease as the axial force changed from compression to tension at large deformation stage. As shown in the figure, even the axial force in tension (catenary action kicked in), the M-N curves agreed with the theoretical ones well.

Assessment of the accuracy of existing CAA models

As a favorable alternate load path to resist progressive collapse due to its low demand in deformation, CAA has been widely studied theoretically. Based on plastic theory, Park and Gamble (2000) proposed a classical model to calculate the CMA in RC slabs. The Park and Gamble (2000)'s model can be further used to predict CAA capacity in RC beam as the CMA and CAA share similar merits. As shown in Fig. 24, the CAA capacity P can be given as:

$$P_{CAA} = \frac{2\left(M_s + M_m - N\delta\right)}{\beta L} \qquad (7)$$

where M_s and M_m are the bending moments at the beam-column interface; N is the axis force in beam; L is the total span of the double-bay beam; β is the ratio of the net span to the total span L, which is 0.5 here; δ is the vertical displacement in the middle column stub. After stringent derivation, which can be found in Park and Gamble (2000) in detail, P can be expressed as:

$$\begin{aligned} P_{CAA} = \frac{2}{\beta L}\Bigg\{ & 0.85 f_c' \beta_1 hb\left[\frac{h}{2}\left(1-\frac{\beta_1}{2}\right)+\frac{\delta}{4}\left(\beta_1-3\right)+\frac{\beta L^2}{4\delta}\left(\beta_1-1\right)\left(\varepsilon+\frac{2t}{L}\right)\right. \\ & \left.+\frac{\delta^2}{8h}\left(2-\frac{\beta_1}{2}\right)+\frac{\beta L^2}{4h}\left(1-\frac{\beta_1}{2}\right)\left(\varepsilon+\frac{2t}{L}\right)-\frac{\beta_1\beta^2 L^4}{16h\delta^2}\left(\varepsilon+\frac{2t}{L}\right)^2\right] \\ & -\frac{1}{3.4 f_c'}\left(T_s - T_m - T_s' + T_m'\right)^2 + \left(T_s' + T_m'\right)\left(\frac{h}{2}-a_s-\frac{\delta}{2}\right) \\ & +\left(T_s + T_m\right)\left(h_0-\frac{h}{2}+\frac{\delta}{2}\right)\Bigg\} \end{aligned} \qquad (8)$$

and

$$\varepsilon+\frac{2t}{L}=\frac{\left(\frac{1}{hE_cb}+\frac{2}{LK}\right)\left[0.85f_c^{'}\beta_1b\left(\frac{h}{2}-\frac{\delta}{4}-\frac{T_s-T_m-T_s{'}+T_m{'}}{1.7f_c^{'}\beta_1b}\right)+T_m{'}-T_m\right]}{1+0.2125\frac{f_c^{'}\beta_1\beta L^2b}{\delta}\left(\frac{1}{hE_cb}+\frac{2}{LK}\right)} \tag{9}$$

where h and b are the beam depth and beam width, respectively; β_1 is the ratio of the depth of the concrete equivalent rectangular stress block to the depth of neutral-axis; ε is the axial strain of the double-bay beam; t is the axial movement of the side column stub; T_s and T_m are the steel tensile forces at side beam-column interface and middle beam-column interface, respectively; T_s' and T_m' are the steel compressive forces at side beam-column interface and middle beam-column interface, respectively; f_c' is the concrete cylinder compression strength; h_0 is the effective depth of the beam; a_s is the distance from the centroid of compressive steel to the concrete compression surface; E_c is the concrete elastic modulus; K is the lateral stiffness.

To evaluate the accuracy of the model, 45 specimens from existing tests (Su et al.2009, Choi and Kim 2011, Sasani et al. 2011b, FarhangVesali et al. 2013, Valipour et al. 2015a, Yu and Tan 2013b, Yu and Tan 2014, Qian et al. 2015, Alogla et al. 2016, Ren et al. 2016) were used for assessment. Table 4 presents the key parameters and analytical results. As shown in Fig. 25a, the mean value and standard deviation of the ratio of measured CAA capacity to the calculated one based on Park and Gamble (2000) were 1.37 and 0.38, respectively. Thus, Park and Gamble (2000)'s model may underestimate the CAA significantly. Similar conclusions were found by Lu et al. (2018). To reveal the reasons for this underestimation, the measured peak displacements (corresponding CAA capacity) were substituted into the model. As shown in Fig. 25b, the mean value and standard deviation of the ratio of the measured CAA to the calculated one were 1.10 and 0.23, respectively. Therefore, the underestimation of Park's model was mainly due to improperly assumption of the peak displacement as a constant value (δ=0.5h). To improve the accuracy of Park and Gamble (2000)'s model, Lu et al. (2018) conducted comprehensive parametric studies based on validated finite element model (FEM). A regression model of $\delta=0.0005L^2/h$ was proposed by Lu et al. (2018). The calculated peak displacements of the specimens are compared with the measured ones in Table 4. As shown in the table, in general, the measured displacements are larger than the calculated ones, especially for specimens with span-to-depth ratio less than 7, which could be explained as the regression model was mainly calculated based on specimens with larger span-to-depth ratio. As shown in Fig. 25c, relied on Lu et al. (2018)'s model, the mean value and standard deviation of the ratio of the measured CAA to the analytical one was 1.04 and 0.23, respectively. If only look at the specimens with span-to-depth ratio less than 7, the mean value was 1.16. Therefore, the regressed equation is more favorable for specimens with relatively larger span-to-depth ratio (greater than 7). Moreover, if we only look at HSC-series specimens in this study, the calculated CAA capacity of HSC-8, HSC-11, and HSC-13 was 112 %, 114 %, and 114 % of the measured one, respectively. Thus, Lu et al. (2018)'s model may considerably overestimate the CAA capacity for the frames with high strength concrete as the regression model (δ=0.0005L^2/h) did not include the parameter of concrete strength.

Assessment of the accuracy of existing TCA models

As the last line of defense in resisting progressive collapse, TCA is undoubtedly the most important mechanism to provide alternate load path. To effectively predict TCA capacity, Yi et al. (2008), Su et al. (2009), and Yu and Tan (2013b) proposed simplified TCA models. In their models, progressive collapse was assumed to be resisted by the tensile force in beam rebar. However, the contribution of beam rebar for TCA capacity is different in different models. In Yi et al. (2008)'s model, both the top and bottom rebar of beam are deemed to provide resistance. However, in Su et al. (2009)'s model, only the bottom rebars are considered to provide resistance. Conversely, Yu and Tan (2013b) assumed that the TCA capacity is purely provided by the top rebars. In this evaluation study, the deformation capacity of each specimen is assumed to be 10% of the total span of the double-bay beam, in accordance to DoD (2009). The TCA model of Yi et al. (2008), Su et al. (2009) and Yu and Tan (2013b) can be expressed as Eqs. 10 -12, respectively.

$$P_{TCA} = 2\psi(A_{st} f_y + A_{sb} f_y^{'})\sin\alpha \qquad (10)$$

$$P_{TCA} = 2A_{sb} f_y^{'} \sin\varphi \quad (11)$$

$$P_{TCA} = 2A_{st} f_y \sin\alpha \quad (12)$$

where A_{st} and A_{sb} are the area of top and bottom rebars, respectively; f_y and f_y' are the yield strength of top and bottom rebars, respectively; ψ is a strain adjustment coefficient, and ψ=0.85; α is the chord rotation of beam; φ is the angle between the connection of top rebar at the side column stub and bottom rebar at the middle column stub and the horizontal line.

A database consists of 30 specimens including the tests from literatures (Su et al. 2009, Yu and Tan 2013b, Yu and Tan 2014, Qian et al. 2015, Alogla et al. 2016, Ren et al. 2016) and tested specimens in this study was utilized to validate the reliability of the TCA models mentioned above. Fig. 26 shows the comparison of the measured TCA capacity with the calculated one. As shown in the figure, the mean ratio of the measured TCA capacity to the calculated one based on the models of Yi et al. (2008), Su et al. (2009), and Yu and Tan (2013b) was 1.06, 1.43 and 1.60, respectively. The standard deviation was 0.28, 0.42 and 0.53, respectively. Thus, among them, the model of Yi et al. (2008) gives the best prediction. The model of Su et al. (2009) neglected the contribution from top rebars resulted in conservative prediction. However, as the model of Yu et al. (2013b) assuming the bottom rebar was completely fractured, which is not in reality, the model may also underestimate the resistance of TCA significantly.

For HSC-series specimens, the mean value of the ratio of measured TCA capacity to calculate one from the models of Yi et al. (2008), Su et al. (2009), and Yu and Tan (2013b) was 0.94, 1.48 and 1.33, respectively. Therefore, different to the specimens using NSC, Yi et al. (2008)'s model overestimates the TCA capacity of the specimens using HSC slightly. However, as the test data collected from HSC specimens are very few and it is necessary to carry out further tests on HSC RC frames to further support the conclusions.

CONCLUSIONS

Based on the results of the experimental and analytical investigation presented in this paper, the following conclusions are drawn:

1. Test results indicated that for normal strength concrete frames, the CAA capacity and TCA capacity increase by 79.0 % and 8.6 %, respectively, when the span-to-depth ratio decreased from 13 to 8. For the frames with high strength concrete, the CAA capacity and TCA capacity, increase by 89.5 % and 13.9 % respectively, when the span-to-depth ratio decreased from 13 to 8. Therefore, the span-depth-ratio has significant effect on CAA capacity but not for TCA capacity.
2. Based on the test results, high strength concrete could increase the CAA capacity of the frame with span-to-depth ratio of 8, 11, and 13 by 18. 2 %, 15.4 %, and 11.6 %, respectively. Thus, high strength concrete is beneficial to enhance CAA capacity, especially for the frames with low span-to-depth ratio. However, the TCA capacity of specimen HSC-8, HSC-11, and HSC-13 only achieved 93.2 %, 87.2 %, and 88.9 % of that of NSC-8, NSC-11, and NSC-13, respectively. Thus, the specimens with high strength concrete may detriment the TCA capacity due to high bond strength between reinforcements and concrete, which prone to premature the fracture of reinforcements. However, it should be noted that non-seismically designed specimens were tested. For seismically designed and detailed specimens, more tests should be carried out on evaluation of the HSC effects.
3. Analytical evaluation indicated that Park's model will underestimate the CAA capacity significantly due to improperly assumption of the peak displacement as $0.5h$. However, the agreements could be improved for both NSC and HSC specimens significantly when the peak displacement assumes to be $0.0005L^2/h$, in accordance to the study of Lu et al. (2018). However, the model proposed by Lu et al. (2018) is more suit for RC frames with relatively larger span-to-depth ratio (larger than 7). And Lu et al. (2018)'s model may overestimate the CAA capacity of HSC-series specimens significantly due to the regression model did not included the effects of concrete strength.

4. Although Yi et al. (2008)'s model produced the best prediction for TCA capacity, it slightly underestimates the TCA capacity of NSC frames but overestimate that of HSC frames. Although the models proposed by Yu and Tan (2013b) and Su et al. (2009) underestimate the TCA capacity, the reason was different. For Su et al. (2009), the contribution of top reinforcement is ignored, which disagrees with the test observation. However, for Yu and Tan (2013b), the contribution of bottom reinforcements is neglected, which is over-conservative. In reality, the bottom reinforcement may not fracture completely when the deformation reached 10 % of the total length of the double-span beams, which is proposed by the guideline of DoD (2009).

FUTURE RESEARCH

Based on the test results and conclusions, the future research needed was highlighted. The effects of HSC on seismically designed specimens should be evaluated in the future as the conclusions from non-seismically designed specimens may not be suitable for seismically designed ones. Moreover, the effects of different boundary conditions (different column missing scenarios) should be quantified. Furthermore, the effects of HSC on dynamic response of RC moment frame subjected to suddenly column removal should be investigated.

DATA AVAILABILITY

Some or all data, models, or code generated or used during the study are available from the corresponding author by request (data related in the measured curves, photos, etc.).

REFERENCES

ASCE/SEI 7 (2010) "Minimum Design Loads for Buildings and Other Structures." Structural Engineering Institute-American Society of Civil Engineers, Reston, VA, 424 pp.

ACI Committee 318 (2014), "Building Code Requirements for Structural Concrete (ACI 318-14) and Commentary (318R-14)." American Concrete Institute, Farmington Hills, MI, 433 pp.

Alogla, K., Weekes, L., and Augusthus-Nelson, L. (2016) “A New Mitigation Scheme to Resist Progressive Collapse of RC Structures.” *Construction and Building Materials*, 125: pp. 533–545.

BS8110 (1997), “Structural Use of Concrete Part 1: Code of Practice for Design and Construction.” British Standard Institute, United Kingdom.

British Standards Institute (2006), “Eurocode 1: Actions on Structures. Part 1-7: General Actions-Accidental Actions.” BS EN 1991-1-7: 2006, London.

Choi, H., and Kim, J. (2011). “Progressive Collapse-Resisting Capacity of RC Beam–Column Sub-assemblage.” *Magazine of Concrete Research*, 63(4): pp. 297–310.

DoD (2009). “Design of Building to Resist Progressive Collapse.” Unified Facility Criteria, UFC 4-023-03, U.S. Department of Defense, Washington, DC.

FarhangVesali, N., Valipour, H., Samali, B., and Foster, S. (2013). “Development of Arching Action in Longitudinally-Restrained Reinforced Concrete Beams.” *Construction and Building Materials*, 47: pp. 7-19.

GSA (2009). “Progressive Collapse Analysis and Design Guidelines for New Federal Office Buildings and Major Modernization Projects.” U.S. General Service Administration, Washington, DC.

Izzuddin, B. A., Vlassis, A. G., Elghazouli, A. Y., and Nethercot, D. A. (2008). “Progressive Collapse of Multi-Storey Buildings due to Sudden Column Loss—Part I: Simplified Assessment Framework.” *Engineering Structures,* 30(5): pp. 1308–1318.

Kim, J., and An, D. (2009). “Evaluation of Progressive Collapse Potential of Steel Moment Frames Considering Catenary Action.” *The Structural Design of Tall and Special Buildings*, 18(4): pp. 455-465.

Kim, J., Choi, H., and Min, K.W. (2011). “Use of Rotational Friction Dampers to Enhance Seismic and Progressive Collapse Resisting Capacity of Structures.” *The Structural Design of Tall and Special Buildings,* 20(4): pp.515-537.

Kim, J., and Choi, H. (2016). “Monotonic Loading Tests of RC Beam-Column Subassemblage Strengthened to Prevent Progressive Collapse.” *International Journal of Concrete Structures and Materials,* 9(4): pp. 401-413.

Lew, H. S., Bao, Y. H., Pujol, S., and Sozen, M. A. (2014). “Experimental Study of Reinforced Concrete Assemblies under Column Removal Scenario.” *ACI Structural Journal,* 111(4): pp. 881-892.

Lu, X. Z., Lin, K. Q., Li, Y., Guan, H., Ren, P. Q., and Zhou, Y. L. (2017). “Experimental Investigation of RC Beam-Slab Substructures against Progressive Collapse Subject to an Edge-Column Removal Scenario.” *Engineering Structures*, 149: pp. 91-103.

Lu, X. Z., and Li, K. Q., Li, C. F., and Li, Y. (2018). “New Analytical Calculation Models for Compressive Arch Action in Reinforced Concrete Structures.” *Engineering Structures*, 168: pp. 721-735.

Orton, S., Jirsa, J. O., and Bayrak, O. (2009). “Carbon Fiber-Reinforced Polymer for Continuing in Existing Reinforced Concrete Buildings Vulnerable to Collapse.” *ACI Structural Journal*, 106(5): pp. 608-616.

Park, R., and Gamble, W. L. (2000). “Reinforced Concrete Slabs.” Wiley, New York.

Peng, Z. H., Orton, S. L., Liu, J. R., and Tian, Y. (2017). “Experimental Study of Dynamic Progressive Collapse in Flat-Plate Buildings subjected to Exterior Column Removal.” *Journal of Structural Engineering,* 143(9): 04017125.

Qian, K. and Li, B. (2012a). “Slab Effects on the Response of Reinforced Concrete Substructures after Loss of Corner Column.” *ACI Structural Journal,* 109(6): pp. 845-855.

Qian, K., and Li, B. (2012b). “Dynamic Performance of RC Beam-Column Substructures under the Scenario of the Loss of a Corner Column—Experimental Results.” *Engineering Structures,* 42: pp. 154-167.

Qian, K., and Li, B. (2012c). “Experimental and Analytical Assessment on RC Interior Beam-Column Subassemblages for Progressive Collapse.” *Journal of Performance of Constructed Facilities*, ASCE, 26(5): pp. 576-589.

Qian, K., and Li, B. (2015a). “Quantification of Slab Influence on the Dynamic Performance of RC Frames against Progressive Collapse.” *Journal of Performance of Constructed Facilities*, ASCE, 29(1): 04014029.

Qian, K., and Li, B. (2015b). “Research Advances in Design of Structures to Resist Progressive Collapse.” *Journal of Performance of Constructed Facilities*, ASCE, 29(5): B4014007.

Qian, K., Li, B., and Ma, J.-X. (2015). “Load-Carrying Mechanism to Resist Progressive Collapse of RC Buildings.” *Journal of Structural Engineering*, 141(2): 04014107.

Qian, K., Li, B., and Zhang, Z. (2016). “Influence of Multicolumn Removal on the Behavior of RC Floors.” *Journal of Structural Engineering*, 142(5): 04016006.

Qian, K., and Li, B. (2017). “Effects of Masonry Infill Wall on the Performance of RC Frames to Resist Progressive Collapse.” *Journal of Structural Engineering,* 143(9): 04017118.

Qian, K., Liu, Y., Yang, T., and Li, B. (2018). “Progressive Collapse Resistance of Posttensioned Concrete Beam-Column Subassemblages with Unbonded Posttensioning Strands.” *Journal of Structural Engineering,* 144(1): 04017182.

Qian, K., Weng, Y. H., and Li, B. (2019). “Improving Behavior of Reinforced Concrete Frames to Resist Progressive Collapse through Steel Bracings.” *Journal of Structural Engineering,* 145(2): 04018248.

Ren, P. Q., Li, Y., Lu, X. Z., Guan, H., and Zhou, Y. L. (2016). “Experimental Investigation of Progressive Collapse Resistance of One-Way Reinforced Concrete Beam-Slab Substructures under a Middle-Column-Removal Scenario.” *Engineering Structures,* 118: pp. 28–40.

Su, Y. P., Tian, Y., and Song, X. S. (2009). “Progressive Collapse Resistance of Axially-Restrained Frame Beams.” *ACI Structural Journal*, 106(5): pp. 600-607.

Sasani, M., Kazemi, A., Sagiroglu, S., and Forest, S. (2011a). “Progressive Collapse Resistance of an Actual 11-Story Structure Subjected to Severe Initial Damage.” *Journal of Structural Engineering*, 137(9): pp. 893-902.

Sasani, M., Werner, A., and Kazemi, A. (2011b) “Bar Fracture Modeling in Progressive Collapse Analysis of Reinforced Concrete Structures.” *Engineering Structures*, 33(2): pp. 401–409.

Tsai, M. H. (2010). “An Analytical Methodology for the Dynamic Amplification Factor in Progressive Collapse Evaluation of Building Structures.” *Mechanics Research Communications*, 37(1): pp. 61-66.

Valipour, H., Vessali, N., Foster, S.J., and Samali, B. (2015a). "Influence of Concrete Compressive Strength on the Arching Behaviour of Reinforced Concrete Beam Assemblages." *Advances in Structural Engineering*, 18(8): pp. 1199-1214.

Valipour, H., Vessali, N., and Foster, S.J. (2015b). “Fibre-reinforced Concrete Beam Assemblage Subject to Column Loss.” *Magazine of Concrete Research*, 68 (6): pp. 305-317.

Valipour, H., Rajabi, A., Foster, S.J., and Bradford, M. A. (2015c). “Arching Behavior of precast Concrete Slabs in a Deconstructible Composite Bridge Deck.” *Construction and Building Materials,* 87: pp. 67-77.

Xiao, Y., Kunnath, S., Li, F. W., Zhao, Y. B., Lew, H. S., and Bao, Y. (2015). “Collapse Test of Three-Story Half-Scale Reinforced Concrete Frame Building.” *ACI Structural Journal*, 112(4): pp. 429-438.

Yi, W. J., He, Q. F., Xiao, Y., and Kunnath, S. K. (2008). “Experimental Study on Progressive Collapse-Resistant Behavior of Reinforced Concrete Frame Structures.” *ACI Structural Journal*, 105(4): pp. 433-439.

Yap, L. S., and Li, B. (2011). “Experimental Investigation of Reinforced Concrete Exterior Beam-Column Subassemblages for Progressive Collapse.” *ACI Structural Journal,* 108(5): pp. 542-552.

Yu, J., and Tan, K. H. (2013a). “Experimental and Numerical Investigation on Progressive Collapse Resistance of Reinforced Concrete Beam Column Sub-assemblages.” *Engineering Structures*, 55: pp. 90-106.

Yu, J., Tan, K. H. (2013b). “Structural Behavior of RC Beam-Column Sub-assemblages under a Middle Column Removal Scenario.” *Journal of Structural Engineering*, 139(2): pp. 233–250.

Yu, J., and Tan, K. H. (2014). “Special Detailing Techniques to Improve Structural Resistance against Progressive Collapse.” *Journal of Structural Engineering*, 140(3): 04013077.

Yu, J., Rinder, T., Stolz, A., Tan, K. H., and Riedel, W. (2014). “Dynamic Progressive Collapse of an RC Assemblage Induced by Contact Detonation.” *Journal of Structural Engineering*, 140(6): 04014014.

FIGURE CAPTIONS

Fig. 1. Dimension and reinforcement details of Specimen NSC-11: (a) elevation view; (b) cross sections

Fig. 2. Test setup and instrumentation layout of the tests: (a) photo; (b) schematic view

Fig. 3. Vertical load-displacement history: (a) NSC-series; (b) HSC-series

Fig. 4. Crack pattern: (a) NSC-11; (b) HSC-11

Fig. 5. Failure mode of Specimen NSC-11

Fig. 6. Failure mode of Specimen NSC-13

Fig. 7. Failure mode of Specimen NSC-8

Fig. 8. Failure mode of Specimen HSC-11

Fig. 9. Failure mode of Specimen HSC-13

Fig. 10. Failure mode of Specimen HSC-8

Fig. 11. Horizontal reaction force-displacement curves: (a) NSC series; (b) HSC series

Fig. 12. Deformation shape of the beams of Specimen NSC-11 at various stages

Fig. 13. Strain gauge results of NSC-11: (a) top beam rebar; (b) bottom beam rebar

Fig. 14. Strain gauge results of HSC-11: (a) top beam rebar; (b) bottom beam rebar

Fig. 15. Strain gauge results of HSC-8: (a) top beam rebar; (b) bottom beam rebar

Fig. 16. Dynamic performance of the specimens

Fig. 17. Relationship of internal forces and the load resistance

Fig. 18. Collapse Resistance contributions from axial and shear force: (a) NSC-11; (b) HSC-11; (c) NSC-8; (d) HSC-8

Fig. 19. Variations of bending moments v.s. deflections at different cross-section: (a) NSC-11; (b) HSC-11; (c) NSC-8; (d) HSC-8

Fig. 20. M-N relationship at the beam end of NSC-11: (a) nearby the middle column; (b) nearby the side column

Fig. 21. M-N relationship at the beam end of NSC-8: (a) nearby the middle column; (b) nearby the side column

Fig. 22. M-N relationship at the beam end of HSC-11: (a) nearby the middle column; (b) nearby the side column

Fig. 23. M-N relationship at the beam end of HSC-8: (a) nearby the middle column; (b) nearby the side column

Fig. 24. Internal Force diagram for derivation of the analytical model of CAA

Fig. 25. Comparison of the measured CAA capacity with calculated one: (a) δ=0.5h; (b) measured δ; (c) $\delta=0.0005L^2/h$

Fig. 26. Comparison of the measured TCA capacity with calculated one: (a) Yi et al. (2008); (b) Su et al. (2009); (c) Yu and Tan (2013b)

Table 1-Specimen properties

Test ID	Beam clear span (mm)	Beam longitudinal reinforcement				Concrete
		A-A section		B-B section		
		Top	Bottom	Top	Bottom	
NSC-8	2000	3T12	2T12	2T12	2T12	Normal strength
NSC-11	2750	3T12	2T12	2T12	2T12	Normal strength
NSC-13	3250	3T12	2T12	2T12	2T12	Normal strength
HSC-8	2000	3T12	2T12	2T12	2T12	High strength
HSC-11	2750	3T12	2T12	2T12	2T12	High strength
HSC-13	3250	3T12	2T12	2T12	2T12	High strength

Table 2-Material properties of reinforcements

Items		Nominal diameter (mm)	Yield strength (MPa)	Ultimate strength (MPa)	Elongation (%)
Transverse reinforcement	R6	6	348	486	25.4
Longitudinal	T12	12	438	577	16.6
Reinforcements	T16	16	442	605	16.0

Note: R6 represents plain bar of with diameter of 6 mm; T12 and T16 represent deformed rebar with diameter of 12 mm and 16 mm, respectively.

Table 3-Test results

Test ID	Critical displacements (mm)			Critical loads (kN)			MHCF (kN)	MHTF (kN)
	YL	CAA	TCA	YL	CAA	TCA		
NSC-8	25	79	581	53	77	88	-202	147
NSC-11	36	90	712	37	52	94	-178	154
NSC-13	45	108	731	33	43	81	-153	148
HSC-8	16	80	547	56	91	82	-321	145
HSC-11	28	74	663	42	60	80	-259	142
HSC-13	35	104	701	36	48	72	-233	150

Note: YL means yielding load capacity; CAA represents CAA capacity; TCA represents TCA capacity; MHCF means maximum horizontal compressive force; and MHTF means maximum horizontal tensile force.

Table 4-Summary of key parameters and analytical results of CAA

Test	ID	Lateral stiffness (kN/m)	Total length (mm)	Span to depth ratio	Beam section	Beam rebar		Material properties		Test results		Calculated results			
					h×b (mm×mm)	Top (mm)	Bottom (mm)	f_c' (MPa)	f_y (MPa)	Δ (mm)	P (kN)	Δ_L (mm)	$P_{\delta M}{}^{*}$ (kN)	$P_{\delta L}{}^{\#}$ (kN)	$P_{\delta p}{}^{\$}$ (kN)
This Test	NSC-8	1×10^5	4250	8.0	250×150	3Φ12	2Φ12	31.7	438	78.6	69.2	36.1	69.3	79.2	57.1
	NSC-11	1×10^5	5750	11.0	250×150	3Φ12	2Φ12	31.1	438	89.8	46.3	66.1	48.4	52.5	42.2
	NSC-13	1×10^5	6750	13.0	250×150	3Φ12	2Φ12	30.5	438	108.1	36.3	91.1	38.1	40.5	35.7
	HSC-8	1×10^5	4250	8.0	250×150	3Φ12	2Φ12	60.5	438	80.4	87.6	36.1	84.5	98.2	70.8
	HSC-11	1×10^5	5750	11.0	250×150	3Φ12	2Φ12	61.2	438	90.3	56.8	66.1	59.2	65.0	52.3
	HSC-13	1×10^5	6750	13.0	250×150	3Φ12	2Φ12	59.3	438	103.8	43.6	91.1	46.6	49.6	43.7
Su et al. (2009)	A1	1×10^6	2700	4.1	300×150	2Φ12	2Φ12	25.8	350	48.9	168.0	12.2	130.3	145.3	82.3
	A2	1×10^6	2700	4.1	300×150	3Φ12	3Φ12	28.2	350	56.4	221.0	12.2	159.5	180.3	109.9
	A3	1×10^6	2700	4.1	300×150	3Φ14	3Φ14	31.2	340	76.4	246.0	12.2	180.3	215.1	138.3
	A4	1×10^6	2700	4.1	300×150	2Φ12	1Φ14	23.0	350	65.0	147.0	12.2	104.6	126.7	68.0
	A5	1×10^6	2700	4.1	300×150	3Φ12	2Φ12	26.5	350	70.7	198.0	12.2	132.7	160.3	93.9
	A6	1×10^6	2700	4.1	300×150	3Φ14	2Φ14	28.6	340	69.2	226.0	12.2	159.5	188.0	116.8
	B1	1×10^6	4200	6.6	300×150	3Φ14	3Φ14	18.6	340	100.0	125.0	29.4	91.3	107.6	80.8
	B2	1×10^6	5700	9.1	300×150	3Φ14	3Φ14	19.3	340	102.0	82.9	54.2	64.6	75.7	60.0
	B3	1×10^6	5700	9.1	300×150	3Φ14	2Φ14	21.1	340	85.5	74.7	54.2	63.0	68.6	51.8
	C1	1×10^6	2700	6.1	200×100	2Φ12	2Φ14	15.9	350	33.7	60.9	18.2	44.5	46.7	35.7
	C2	1×10^6	2700	6.1	200×100	2Φ12	2Φ12	16.8	350	33.5	64.9	18.2	45.3	47.5	36.0
	C3	1×10^6	2700	6.1	200×100	2Φ12	2Φ12	16.3	350	28.7	68.6	18.2	45.6	47.1	35.8
Choi et al. (2011)	5S	N/A	3315	6.7	225×150	5Φ10	2Φ10	17.0	493	103.0	39.9	24.4	57.6	71.7	57.2
	5G	N/A	3325	8.2	185×150	2Φ10	2Φ10	17.0	493	84.5	22.8	29.9	30.6	48.2	30.3
	8S	N/A	3315	7.7	195×140	5Φ10	3Φ10	30.0	493	59.3	54.1	28.2	70.0	76.6	61.6
	8G	N/A	3325	9.4	160×125	2Φ10	2Φ10	30.0	493	59.0	23.7	34.5	29.4	33.4	26.3
Sasani et al. (2011)	P1	N/A	4170	10.4	190×190	5Φ9.5	2Φ9.5	41.0	516	41.0	71.8	45.8	44.9	60.7	44.1
Yu and Tan (2013b)	S1	1.06×10^5	5750	11.0	250×150	2Φ10 1Φ13	2Φ10	31.2	511	78.0	41.6	66.1	47.9	50.0	39.8
	S2	1.06×10^5	5750	11.0	250×150	3Φ10	2Φ10	31.2	511	73.0	38.4	66.1	45.7	46.9	36.7
	S3	4.29×10^5	5750	11.0	250×150	3Φ13	2Φ10	38.2	511	74.4	54.5	66.1	59.8	61.7	48.1
	S4	4.29×10^5	5750	11.0	250×150	3Φ13	2Φ13	38.2	494	81.0	63.2	66.1	64.9	68.3	54.8
	S5	4.29×10^5	5750	11.0	250×150	3Φ13	3Φ13	38.2	494	74.5	70.3	66.1	75.4	77.4	63.8
	S6	4.29×10^5	5750	11.0	250×150	3Φ16	2Φ13	38.2	494	114.4	70.3	66.1	66.8	78.0	64.4
	S7	4.29×10^5	4550	8.6	250×150	3Φ13	2Φ13	38.2	494	74.4	82.8	41.4	84.5	94.4	69.1

	S8	4.29×10^5	3350	6.2	250×150	3Φ13	2Φ13	38.2	494	45.9	121.3	22.4	128.3	136.6	93.4
Yu and Tan (2014)	F1-CD	4.29×10^5	5750	11.0	250×150	3Φ13	2Φ13	27.5	488	87.0	51.1	66.1	56.8	60.5	50.3
	F2-MR	4.29×10^5	5750	11.0	250×150	3Φ13	2Φ13	27.5	488	51.0	62.8	66.1	63.1	60.5	50.3
FarhangVesali et al. (2013)	1	N/A	4400	11.7	180×180	2Φ10	2Φ10	30.5	620	49.0	40.5	53.8	36.9	36.0	29.4
	2	N/A	4400	11.7	180×180	2Φ10	2Φ10	27.0	620	44.0	35.7	53.8	35.7	34.4	28.5
	3	N/A	4400	11.7	180×180	2Φ10	2Φ10	30.0	620	50.0	41.4	53.8	36.5	35.8	29.3
	4	N/A	4400	11.7	180×180	3Φ10	3Φ10	26.0	620	54.0	40.1	53.8	38.6	38.7	32.9
	5	N/A	4400	11.7	180×180	3Φ10	3Φ10	29.5	620	54.0	41.6	53.8	40.3	40.3	33.9
	6	N/A	4400	11.7	180×180	3Φ10	3Φ10	30.0	620	52.0	39.4	53.8	40.9	34.1	34.0
Qian et al. (2015)	P1	N/A	4000	10.5	180×100	2Φ10	2Φ10	19.9	437	35.8	31.6	44.4	24.6	23.8	19.5
	P2	N/A	2800	9.3	140×80	2Φ10	2Φ10	20.8	437	32.9	35.5	28.0	21.0	21.4	17.7
Valipour et al. (2015a)	No. 1	N/A	4400	11.7	180×180	3Φ10	2Φ10	67.0	480	59.0	51.3	53.8	48.8	47.2	38.0
	No. 2	N/A	4400	11.7	180×180	2Φ10	2Φ10	67.0	480	54.8	42.5	53.8	46.4	43.3	34.1
	No. 3	N/A	4400	11.7	180×180	3Φ10	2Φ10	48.0	480	55.4	47.4	53.8	43.2	41.3	33.4
	No. 4	N/A	4400	11.7	180×180	2Φ10	2Φ10	48.0	480	56.3	38.5	53.8	39.1	37.4	29.5
Ren et al. (2016)	B2	N/A	4000	9.5	175×85	2Φ8 1Φ6	2Φ8	35.2	450	33.0	34	40.0	23.6	22.0	16.6
	B3	N/A	4000	10.9	200×85	2Φ8 1Φ6	2Φ8	35.2	450	33.3	41.0	45.7	30.7	29.7	20.6
Alogla et al. (2016)	SS1	N/A	5750	11.1	250×150	3Φ10	2Φ10	19.4	510	101.0	34.0	66.1	35.1	39.1	32.4
	SS2	N/A	5750	11.1	250×150	3Φ10	2Φ10	19.4	510	96.8	37.9	66.1	35.6	39.1	32.4
	SS3	N/A	5750	11.1	250×150	3Φ10	2Φ10	19.9	510	86.8	37.2	66.1	37.1	39.5	32.6
	SS4	N/A	5750	11.1	250×150	3Φ10	2Φ10	19.9	510	91.4	36.7	66.1	36.5	39.5	32.6

Note: Δ_L represents peak displacement proposed by Lu et al. (2018); $P_{\delta M}{}^{*}$, $P_{\delta L}{}^{\#}$, and $P_{\delta p}{}^{\$}$ represent the calculated CAA capacity in accordance with the measured peak displacement, peak displacement proposed by Lu et al. (2018), and peak displacement proposed by Park and Gamble (2000), respectively.

Figure 1

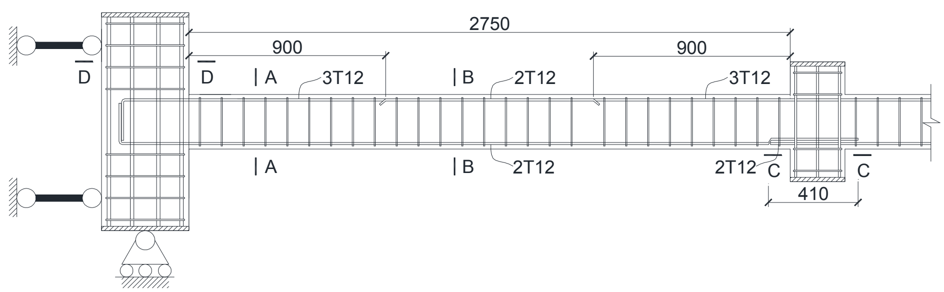
2750
900
900
D
D
A
3T12
B
2T12
3T12
A
B
2T12
2T12
C
C
410

(a)

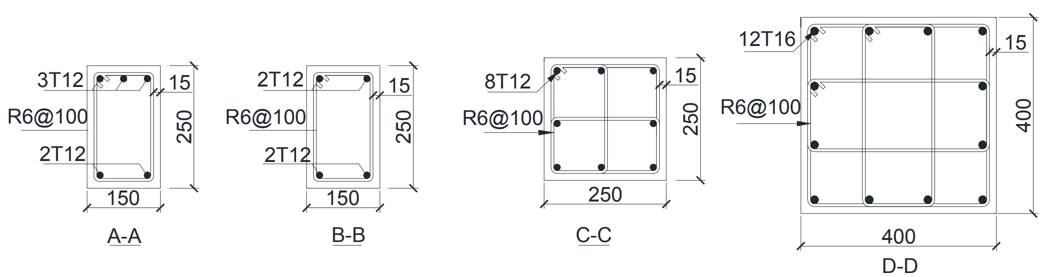
3T12
R6@100
2T12
15
250
150
A-A
2T12
R6@100
2T12
15
250
150
B-B
8T12
R6@100
15
250
250
C-C
12T16
R6@100
15
400
400
D-D

(b)

Figure 2

Click here to access/download;Figure;Figure-2.pdf

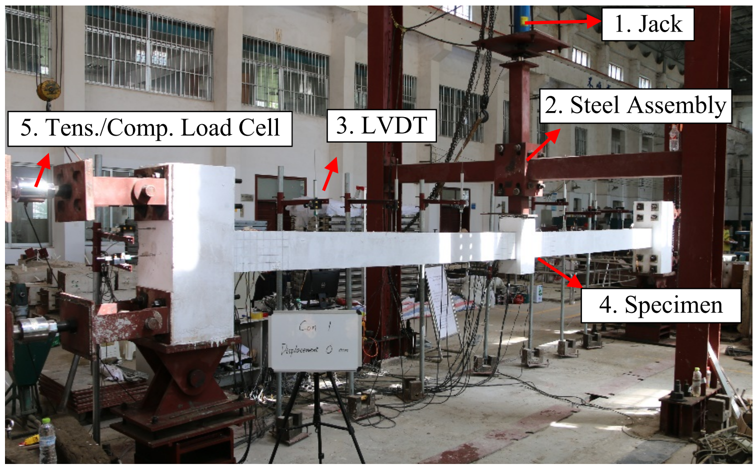

(a)

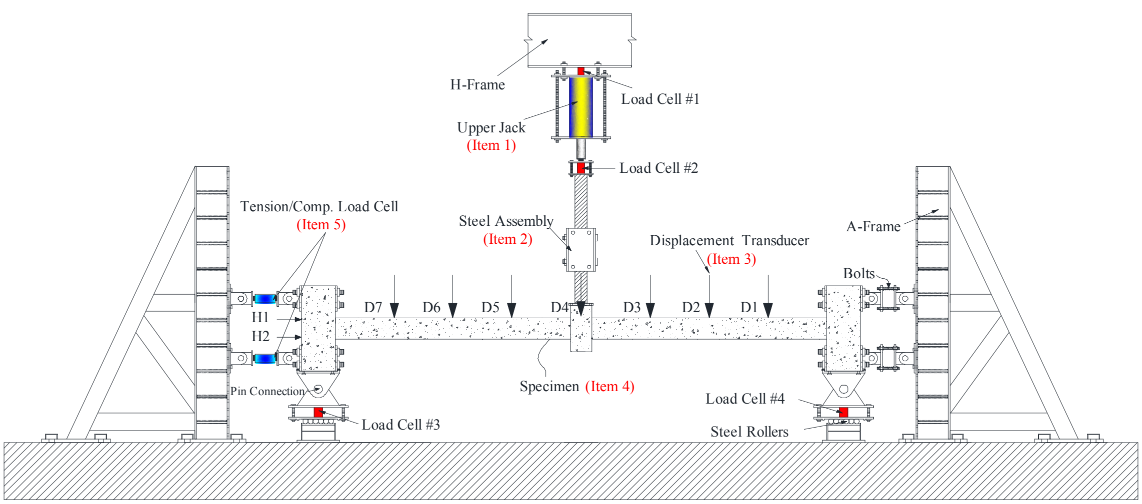

(b)

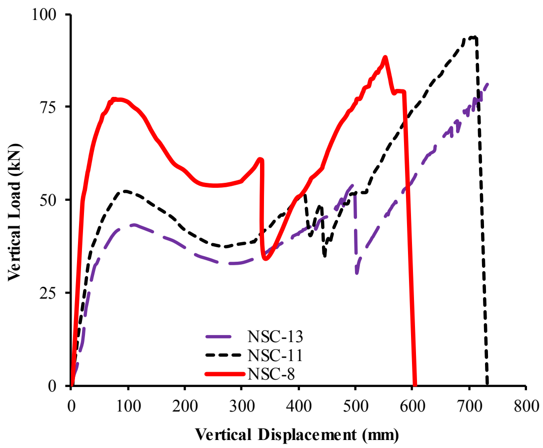

100
75
50
25
0
Vertical Load (kN)
0 100 200 300 400 500 600 700 800
Vertical Displacement (mm)
NSC-13
NSC-11
NSC-8

(a)

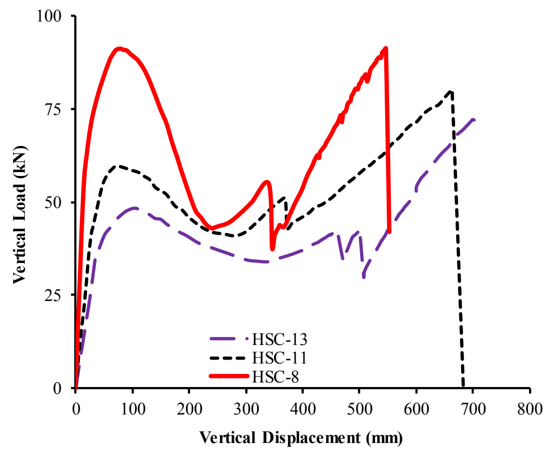

100
75
50
25
0
Vertical Load (kN)
0 100 200 300 400 500 600 700 800
Vertical Displacement (mm)
HSC-13
HSC-11
HSC-8

(b)

Figure 4

Click here to access/download;Figure;Figure-4.pdf

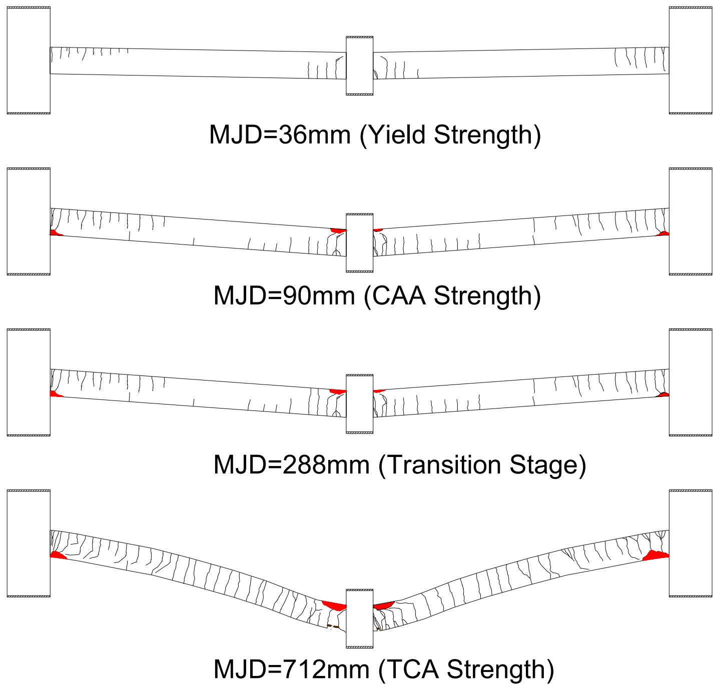

(a)

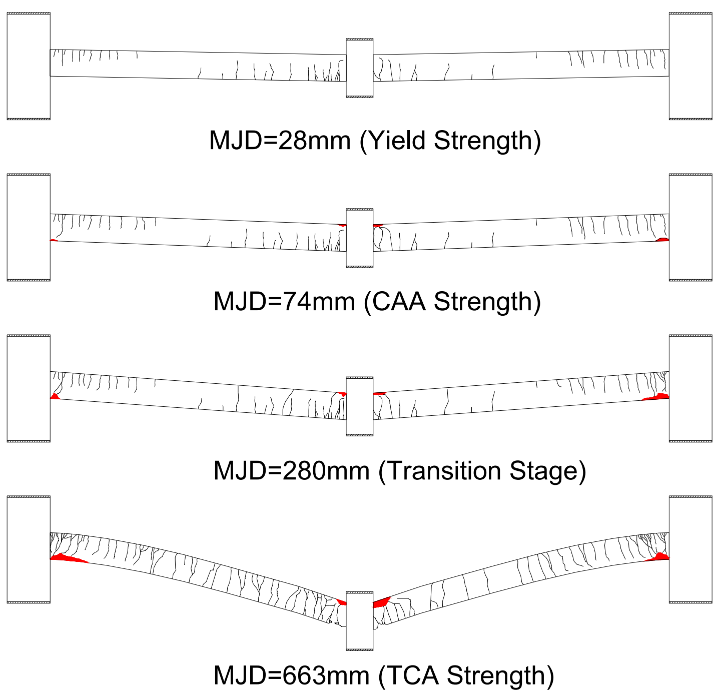

(b)

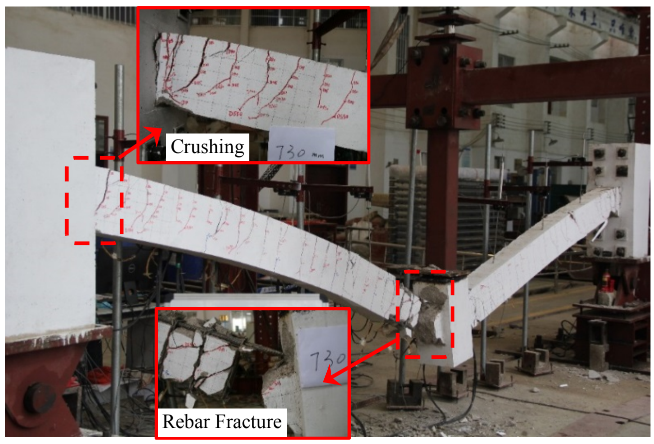
Crushing
730 mm
730
Rebar Fracture

Figure 6

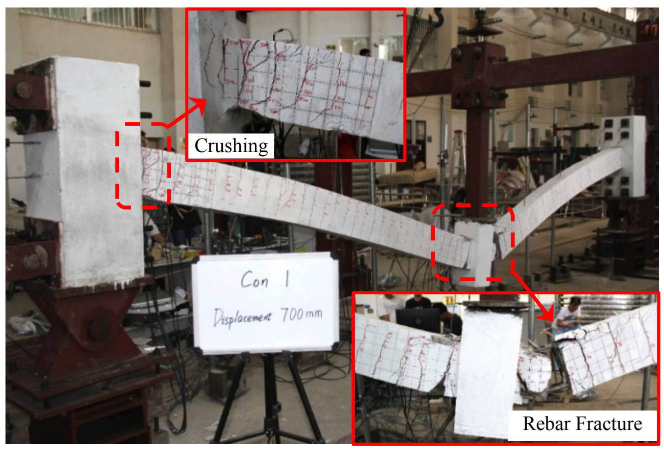

Figure 7

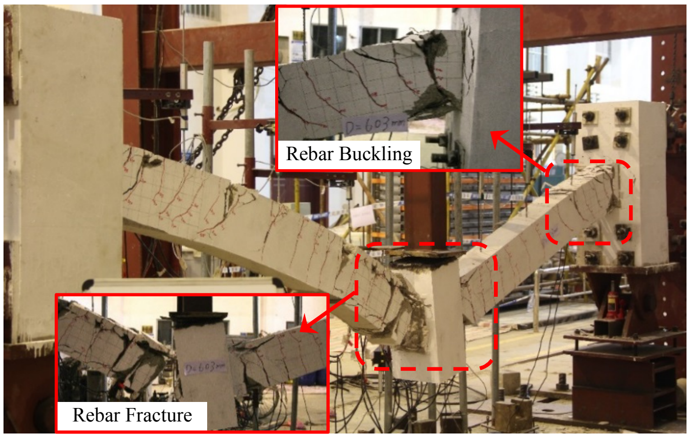

Figure 8

Click here to access/download;Figure;Figure-8.pdf

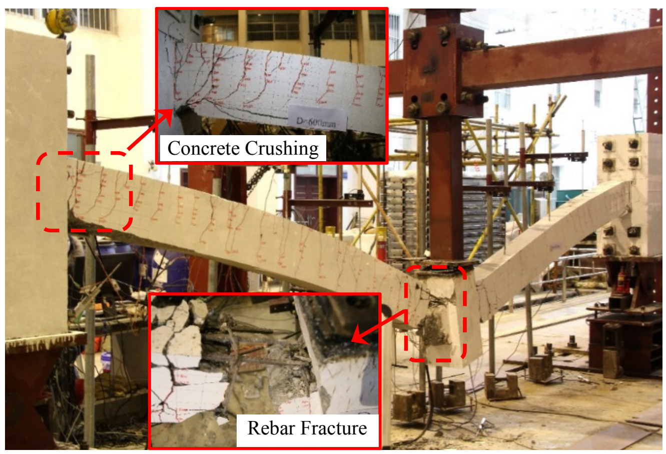

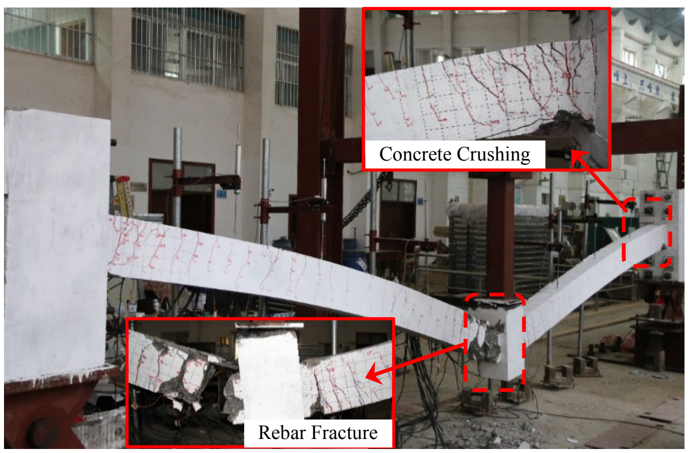
Concrete Crushing
Rebar Fracture

Figure 10

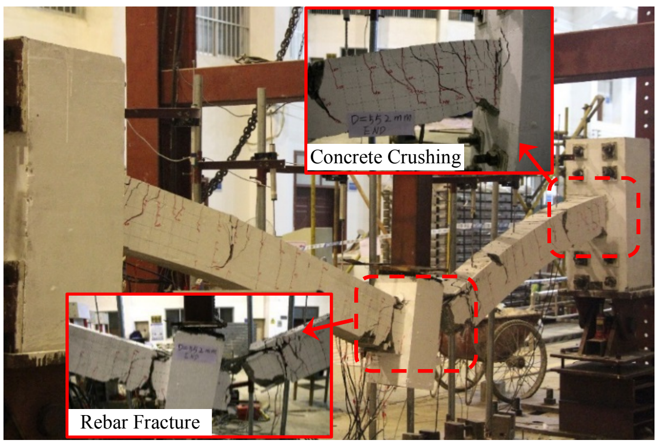

Figure 11

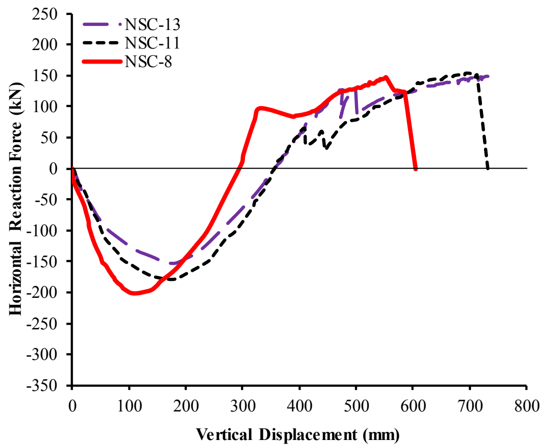

NSC-13
NSC-11
NSC-8
Horizontal Reaction Force (kN)
Vertical Displacement (mm)
250
200
150
100
50
0
-50
-100
-150
-200
-250
-300
-350
0
100
200
300
400
500
600
700
800

(a)

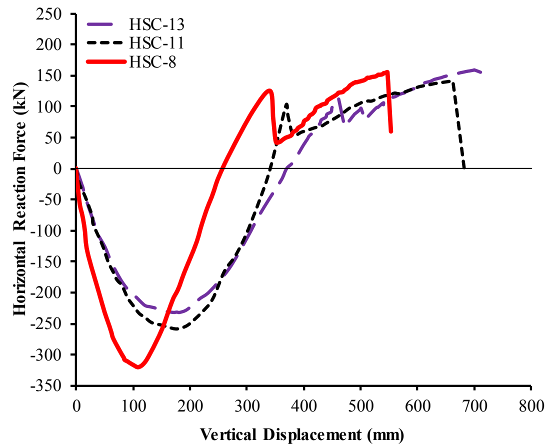

HSC-13
HSC-11
HSC-8
Horizontal Reaction Force (kN)
Vertical Displacement (mm)
250
200
150
100
50
0
-50
-100
-150
-200
-250
-300
-350
0
100
200
300
400
500
600
700
800

(b)

Figure 12

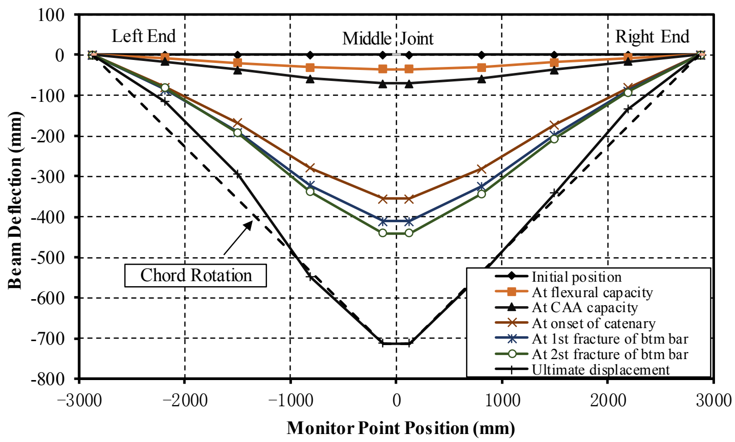

100
0
-100
-200
-300
-400
-500
-600
-700
-800
Beam Deflection (mm)
Left End
Middle Joint
Right End
Chord Rotation
Initial position
At flexural capacity
At CAA capacity
At onset of catenary
At 1st fracture of btm bar
At 2st fracture of btm bar
Ultimate displacement
−3000
−2000
−1000
0
1000
2000
3000
Monitor Point Position (mm)

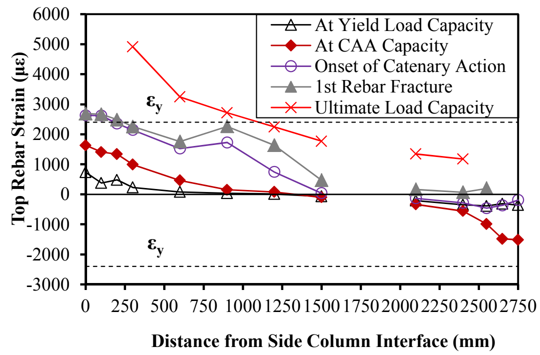

6000
5000
4000
3000
2000
1000
0
-1000
-2000
-3000
Top Rebar Strain (με)
εy
εy
At Yield Load Capacity
At CAA Capacity
Onset of Catenary Action
1st Rebar Fracture
Ultimate Load Capacity
0 250 500 750 1000 1250 1500 1750 2000 2250 2500 2750
Distance from Side Column Interface (mm)

(a)

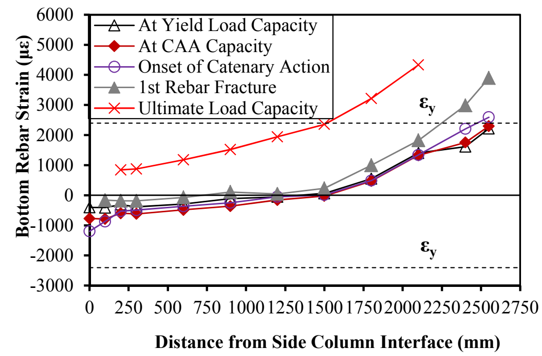

6000
5000
4000
3000
2000
1000
0
-1000
-2000
-3000
Bottom Rebar Strain (με)
εy
εy
At Yield Load Capacity
At CAA Capacity
Onset of Catenary Action
1st Rebar Fracture
Ultimate Load Capacity
0 250 500 750 1000 1250 1500 1750 2000 2250 2500 2750
Distance from Side Column Interface (mm)

(b)

Figure 14

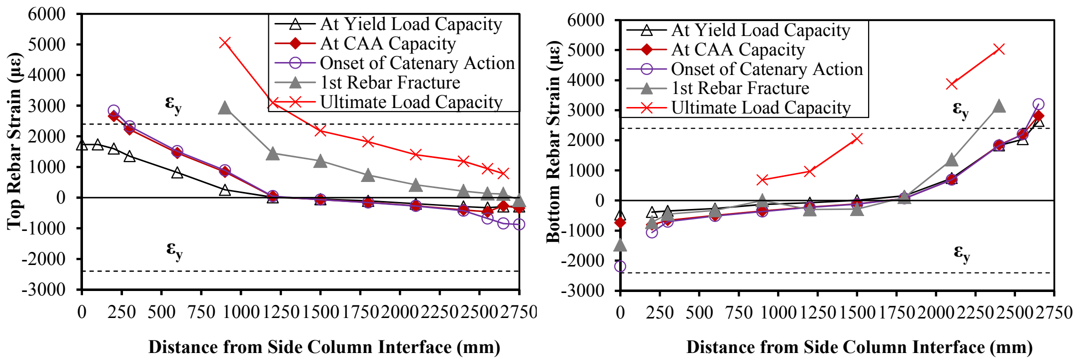

At Yield Load Capacity
At CAA Capacity
Onset of Catenary Action
1st Rebar Fracture
Ultimate Load Capacity
Top Rebar Strain (με)
Bottom Rebar Strain (με)
εy
6000
5000
4000
3000
2000
1000
0
-1000
-2000
-3000
0 250 500 750 1000 1250 1500 1750 2000 2250 2500 2750
Distance from Side Column Interface (mm)

(a)

(b)

Figure 15

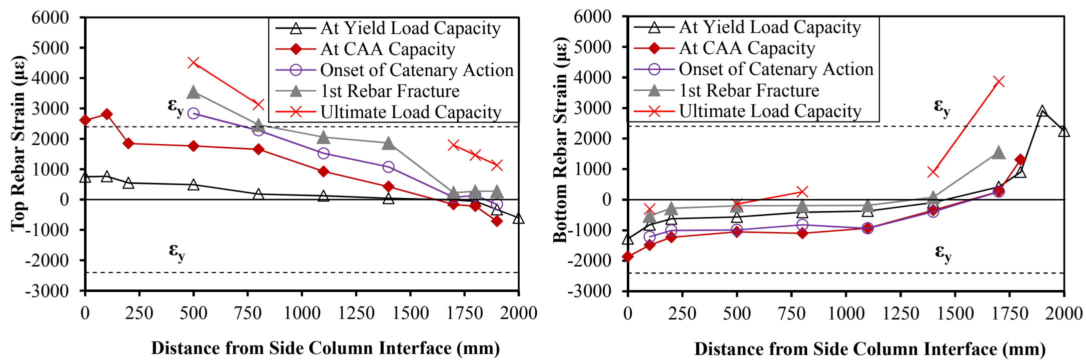

At Yield Load Capacity
At CAA Capacity
Onset of Catenary Action
1st Rebar Fracture
Ultimate Load Capacity
Top Rebar Strain (με)
Bottom Rebar Strain (με)
εy
Distance from Side Column Interface (mm)

(a) (b)

Figure 16

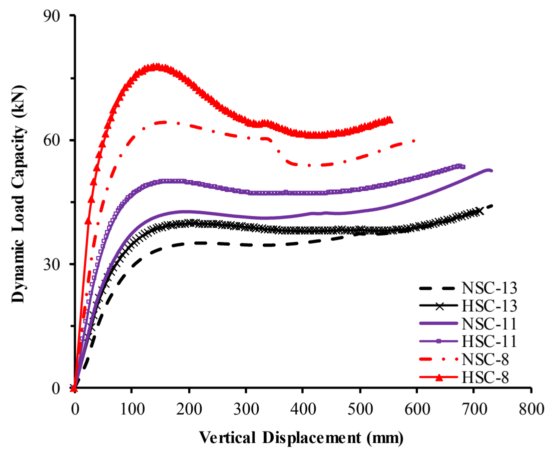

90
60
30
0
Dynamic Load Capacity (kN)
0
100
200
300
400
500
600
700
800
Vertical Displacement (mm)
NSC-13
HSC-13
NSC-11
HSC-11
NSC-8
HSC-8

Figure 17

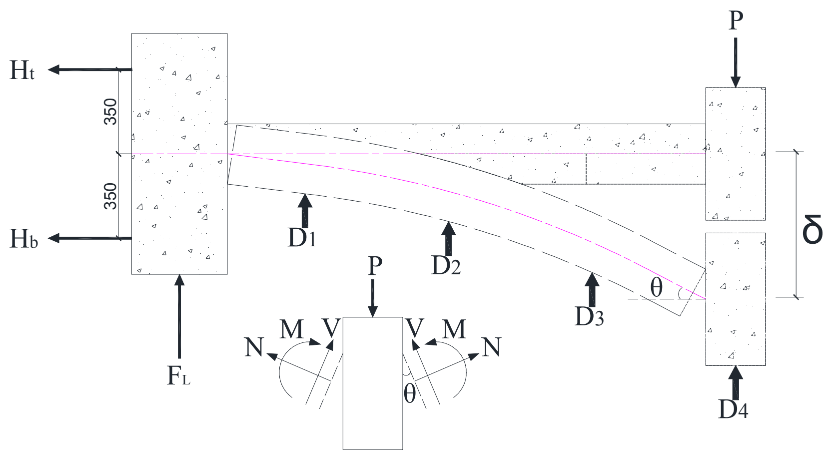

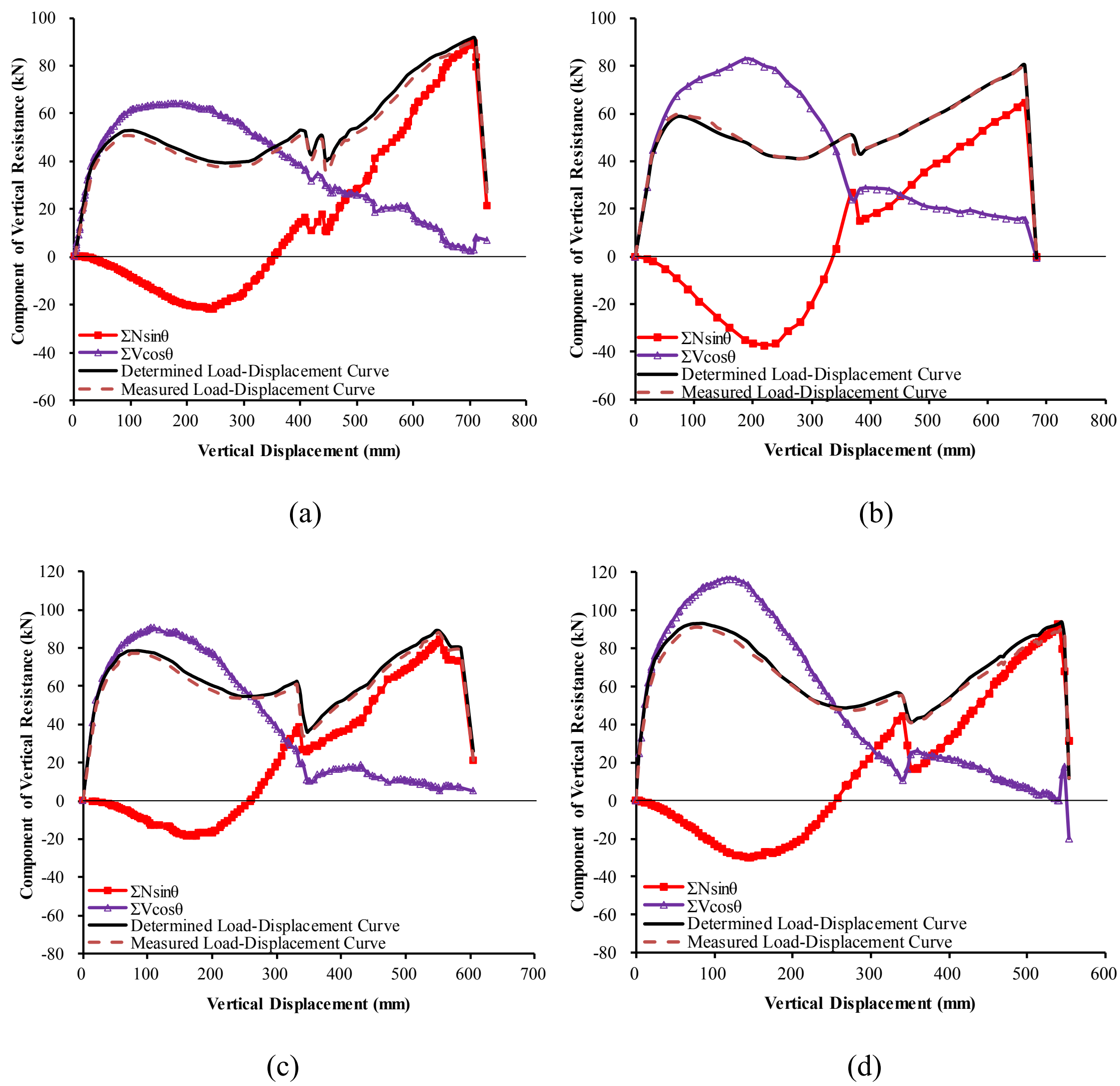
Component of Vertical Resistance (kN)
Vertical Displacement (mm)
ΣNsinθ
ΣVcosθ
Determined Load-Displacement Curve
Measured Load-Displacement Curve
(a)
(b)
(c)
(d)

Figure 19

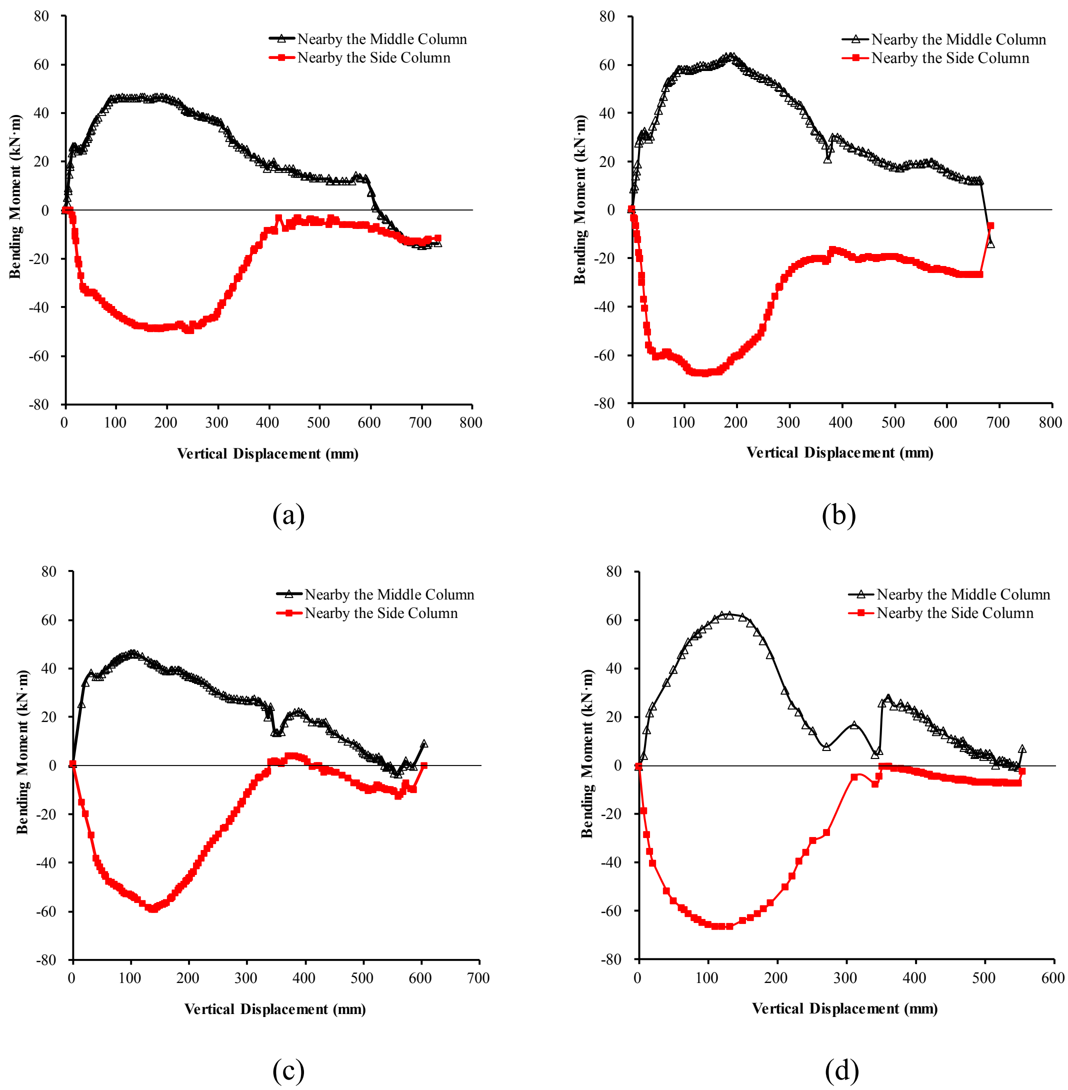
Nearby the Middle Column
Nearby the Side Column
Bending Moment (kN·m)
Vertical Displacement (mm)
(a)
Nearby the Middle Column
Nearby the Side Column
Bending Moment (kN·m)
Vertical Displacement (mm)
(b)
Nearby the Middle Column
Nearby the Side Column
Bending Moment (kN·m)
Vertical Displacement (mm)
(c)
Nearby the Middle Column
Nearby the Side Column
Bending Moment (kN·m)
Vertical Displacement (mm)
(d)

Figure 20

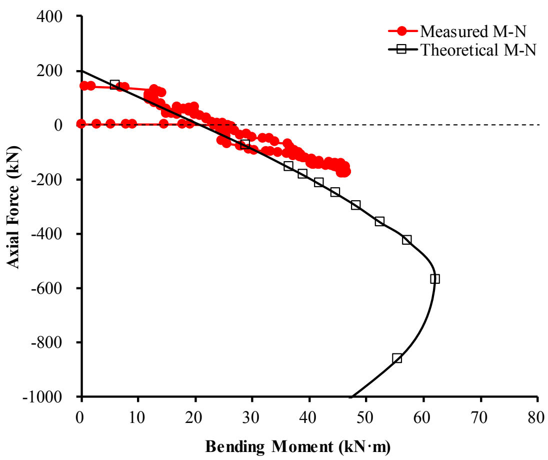
Measured M-N
Theoretical M-N
Axial Force (kN)
Bending Moment (kN·m)
400
200
0
-200
-400
-600
-800
-1000
0
10
20
30
40
50
60
70
80

(a)

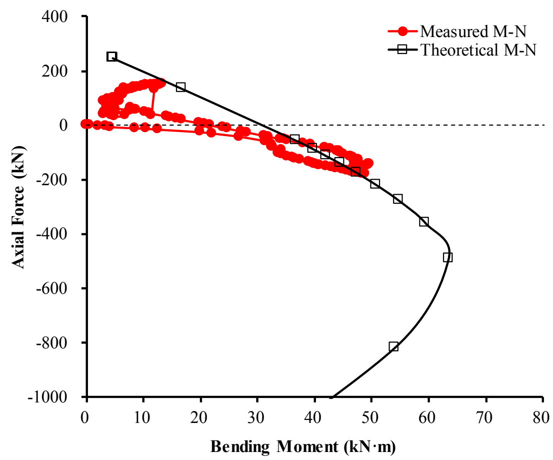
Measured M-N
Theoretical M-N
Axial Force (kN)
Bending Moment (kN·m)
400
200
0
-200
-400
-600
-800
-1000
0
10
20
30
40
50
60
70
80

(b)

Figure 21

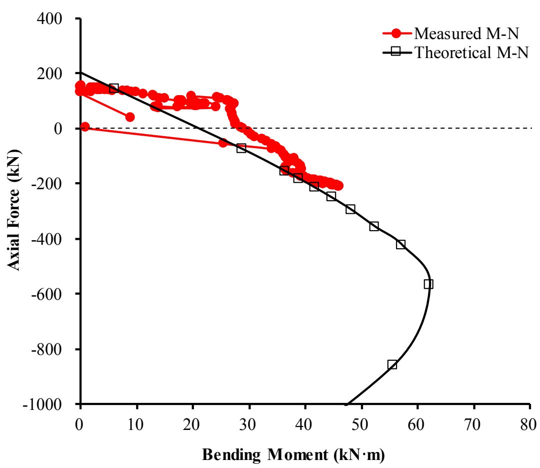
400
200
0
-200
-400
-600
-800
-1000
Axial Force (kN)
0 10 20 30 40 50 60 70 80
Bending Moment (kN·m)
Measured M-N
Theoretical M-N

(a)

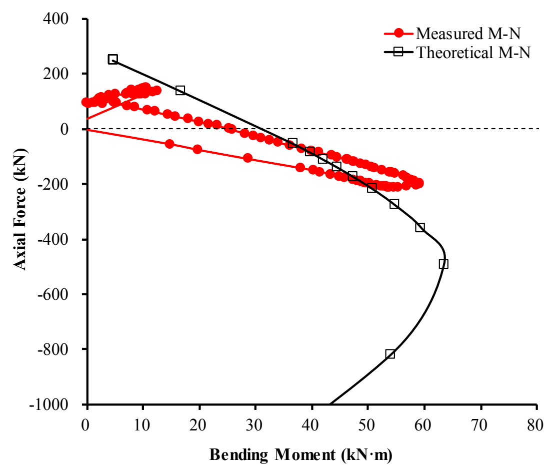
400
200
0
-200
-400
-600
-800
-1000
Axial Force (kN)
0 10 20 30 40 50 60 70 80
Bending Moment (kN·m)
Measured M-N
Theoretical M-N

(b)

Figure 22

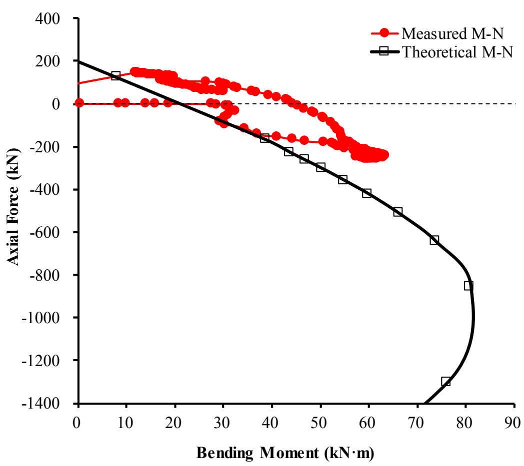

400
200
0
-200
-400
-600
-800
-1000
-1200
-1400
Axial Force (kN)
0 10 20 30 40 50 60 70 80 90
Bending Moment (kN·m)
Measured M-N
Theoretical M-N

(a)

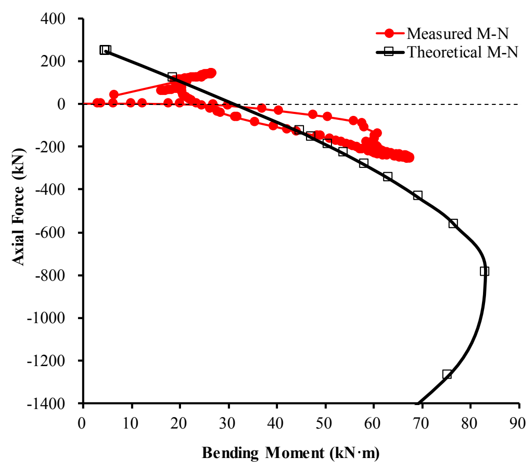

400
200
0
-200
-400
-600
-800
-1000
-1200
-1400
Axial Force (kN)
0 10 20 30 40 50 60 70 80 90
Bending Moment (kN·m)
Measured M-N
Theoretical M-N

(b)

Figure 23

Click here to access/download;Figure;Figure-23.pdf

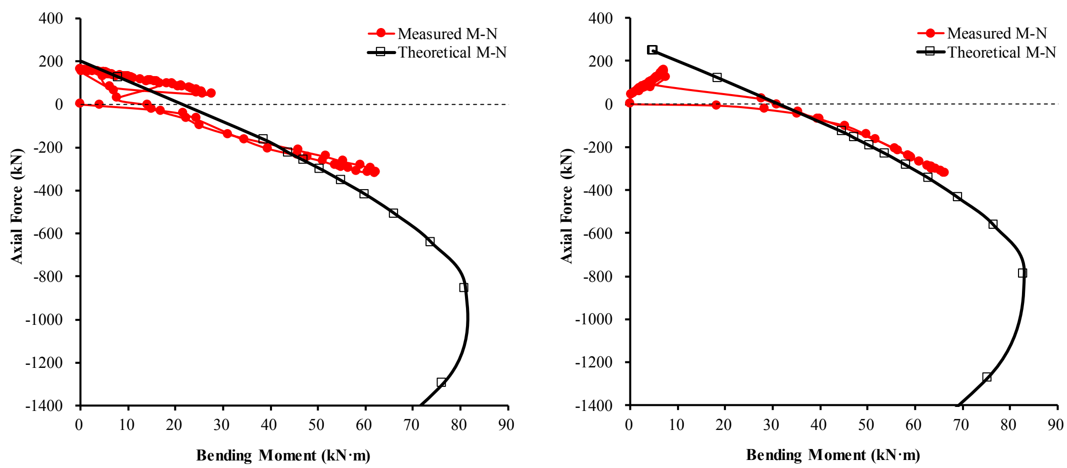

(a) (b)

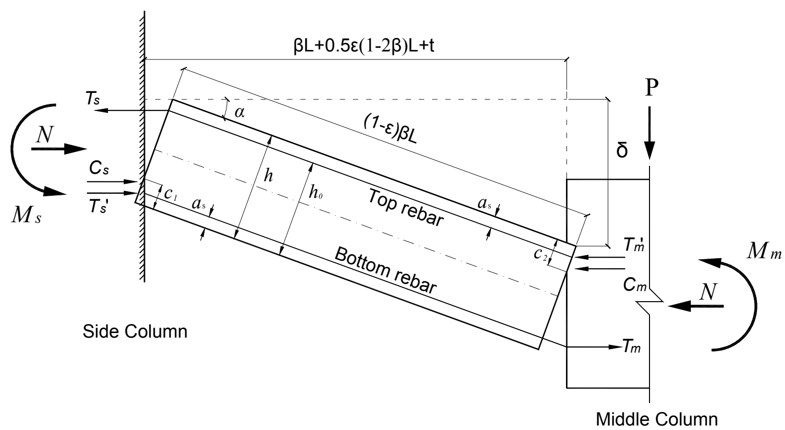
βL+0.5ε(1-2β)L+t
P
T_s
α
(1-ε)βL
δ
N
C_s
T_s'
M_s
c_1
a_s
h
h_0
Top rebar
a_s
c_2
T_m'
M_m
C_m
N
Bottom rebar
T_m
Side Column
Middle Column

Figure 25

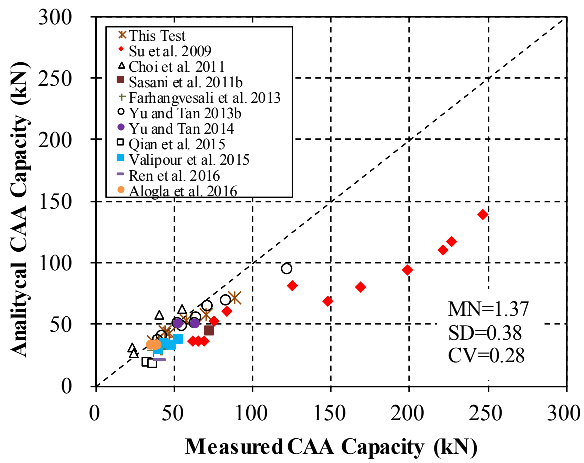

(a)

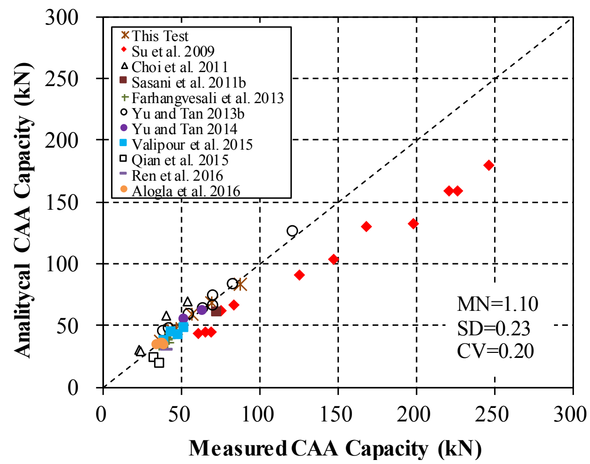

(b)

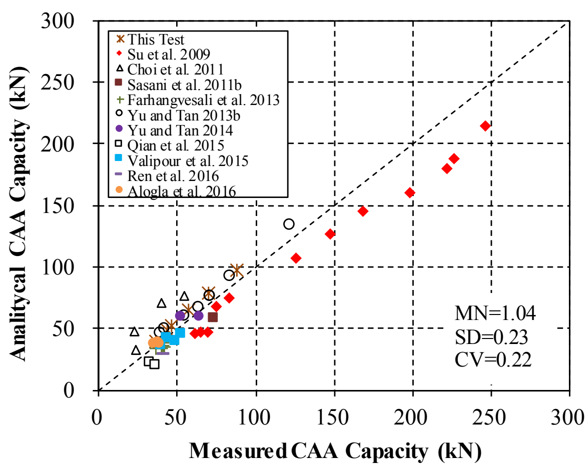

(c)

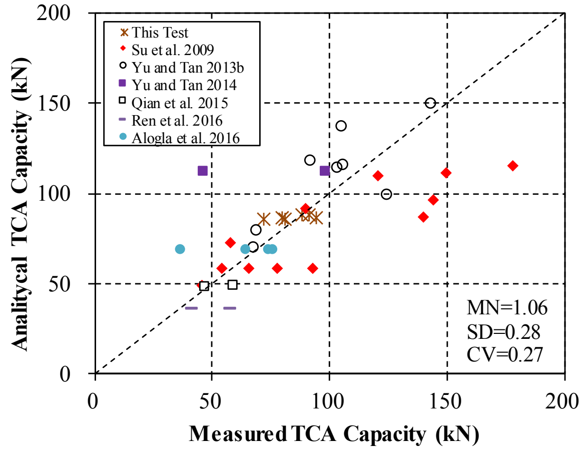
This Test
Su et al. 2009
Yu and Tan 2013b
Yu and Tan 2014
Qian et al. 2015
Ren et al. 2016
Alogla et al. 2016
MN=1.06
SD=0.28
CV=0.27
Analitycal TCA Capacity (kN)
Measured TCA Capacity (kN)

(a)

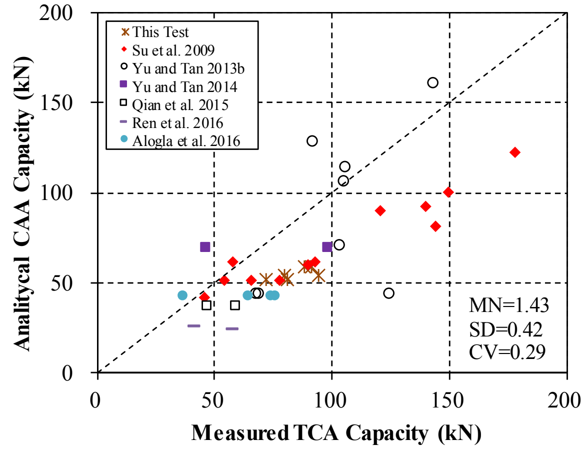
This Test
Su et al. 2009
Yu and Tan 2013b
Yu and Tan 2014
Qian et al. 2015
Ren et al. 2016
Alogla et al. 2016
MN=1.43
SD=0.42
CV=0.29
Analitycal CAA Capacity (kN)
Measured TCA Capacity (kN)

(b)

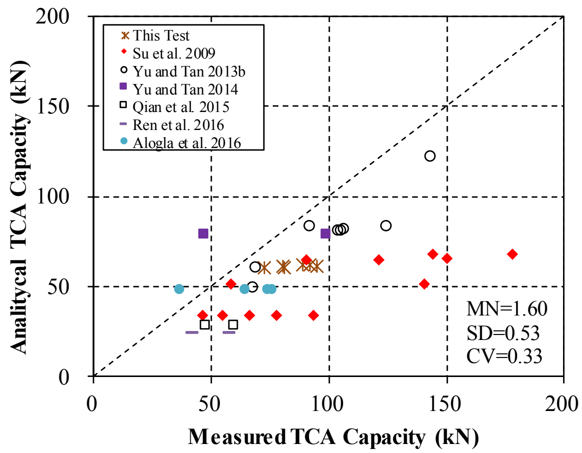
This Test
Su et al. 2009
Yu and Tan 2013b
Yu and Tan 2014
Qian et al. 2015
Ren et al. 2016
Alogla et al. 2016
MN=1.60
SD=0.53
CV=0.33
Analitycal TCA Capacity (kN)
Measured TCA Capacity (kN)

(c)